ACS APPLIED MATERIALS & INTERFACES

Forum Article

www.acsami.org

Importance of Interfaces in Governing Thermal Transport in Composite Materials: Modeling and Experimental Perspectives

Ajit K. Roy,*[,†] Barry L. Farmer,*[,‡] Vikas Varshney,[†,§] Sangwook Sihn,[†,⊥] Jonghoon Lee,[†,§] and Sabyasachi Ganguli[†,⊥]

[†]Thermal Sciences and Materials Branch, Materials and Manufacturing Directorate, Air Force Research Laboratory, Wright-Patterson Air Force Base, Dayton, Ohio 45433-7750, United States

[‡]Materials and Manufacturing Directorate, Air Force Research Laboratory, Wright-Patterson Air Force Base, Dayton, Ohio 45433-7750, United States

[§]Universal Technology Corporation, 1270 N. Fairfield Road, Dayton, Ohio 45432-2600, United States

[⊥]University of Dayton Research Institute, 300 College Park, Dayton, Ohio 45469-0060, United States

Supporting Information

ABSTRACT: Thermal management in polymeric composite materials has become increasingly critical in the air-vehicle industry because of the increasing thermal load in small-scale composite devices extensively used in electronics and aerospace systems. The thermal transport phenomenon in these small-scale heterogeneous systems is essentially controlled by the interface thermal resistance because of the large surface-to-volume ratio. In this review article, several modeling strategies are discussed for different length scales, complemented by our experimental efforts to tailor the thermal transport properties of polymeric composite materials. Progress in the molecular modeling of thermal transport in thermosets is reviewed along with a discussion on the interface thermal resistance between functionalized carbon nanotube and epoxy resin systems. For the thermal transport in fiber-reinforced composites, various micromechanics-based analytical and numerical modeling schemes are reviewed in predicting the transverse thermal conductivity. Numerical schemes used to realize and scale the interface thermal resistance and the finite mean free path of the energy carrier in the mesoscale are discussed in the frame of the lattice Boltzmann–Peierls–Callaway equation. Finally, guided by modeling, complementary experimental efforts are discussed for exfoliated graphite and vertically aligned nanotubes based composites toward improving their effective thermal conductivity by tailoring interface thermal resistance.

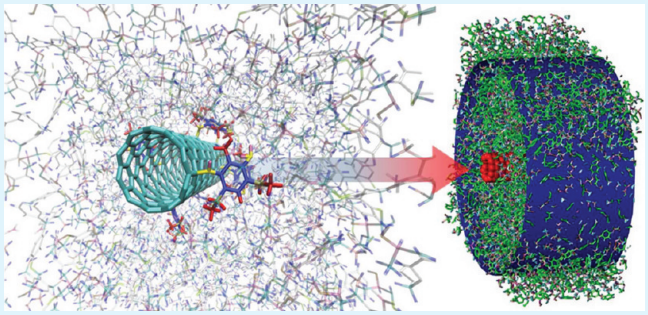

KEYWORDS: *thermal management, interface thermal resistance, multiscale modeling, nanocomposites, thermal conductivity, thermal interface materials*

1. INTRODUCTION

Nonmetallic (polymeric) composites with various forms of fiber reinforcement are extensively used from printed circuit boards to aerospace systems. The thermal loads (excess heat) in all electronic and aerospace systems (aircrafts and spacecrafts) have been steadily increasing at an alarming rate. Traditionally, composites have been used thus far as load-bearing structural components. However, their thermal transport properties (characteristics for transporting thermal load) are inadequate to avert local heating. In view of managing the excess thermal loads generated by thermal devices in aerospace systems, there is an increasing emphasis on tailoring thermal transport properties of composite materials. The anticipated pay-off of improving the thermal properties of composites is primarily in the significant weight savings for the aerospace systems, as compared to metallic materials. As an example, in carbon fiber reinforced polymeric composites, continuous carbon fibers (either in laminated or woven form) are embedded in the polymer matrix. The axial thermal conductivity of carbon fibers is known to be quite high; ranging from 20 W/m-K (for Pan carbon fiber) to 1000 W/m-K for pitch carbon fiber (for example, 900–1000 W/m-K for Thornel K1100 pitch fiber). Thus, the in-plane thermal conductivity of carbon fiber composites (the plane containing the fiber axis) varies between 10 W/m-K to 500 W/m-K, which is significantly high compared to its transverse conductivity (often less than 1 W/m-K. A primary reason for the poor transverse (perpendicular to the fiber axis) thermal conductivity of composites is the fact that the fibers are embedded in a polymeric matrix phase, which is primarily an insulator (whose thermal conductivity is in the range of 0.2–0.3 W/m-K). Furthermore, phonon scattering due to the existence of

Received: October 28, 2011
Accepted: January 17, 2012
Published: February 1, 2012

significant impedance mismatch at the interface between the fiber and the matrix also contributes to the reduction of its transverse thermal conductivity.

To make polymer matrix composites viable for thermal applications, their through-thickness (i.e., perpendicular to the fiber axis) thermal conductivity needs to be significantly enhanced. Thus, it is logical to introduce a conductive phase in the matrix to facilitate thermal pathways to overcome this deficiency. There have been numerous studies of dispersing CNTs in polymers to enhance the thermal conductivity of the polymeric phase.[1−3] The improvements, however, have been very limited, only up to 120%, which do not meet any of the application requirements mentioned earlier. The primary reason of this very limited improvement in the conductivity is due to phonon scattering at the CNT−polymer interface caused by the enormous acoustic mismatch between CNT tips/walls and polymer.[4] Thus, terminating the CNT tips in the polymer is not a viable option for significantly enhancing thermal conductivity in composites through the polymer phase. A possible way to significantly enhance the transverse (i.e., through-thickness) thermal transport in polymer matrix composites is to somehow establish a conductive pathway through the polymer matrix phase between the adjacent fibers.

This article puts forward modeling strategies at various length scales and experimental approaches to address this very question of tailoring the transverse thermal conductivity in polymeric composite materials. The article is divided into four broad sections. First, the fundamental mechanisms of thermal transport in cured epoxy network systems is discussed from an atomistic modeling perspective along with how one can estimate thermal interface resistance at CNT−epoxy interfaces. In the second section, analytical and numerical approaches, based on micromechanical modeling, are presented to address the effective thermal conductivity of fiber-reinforced composites. The third section discusses a mesoscopic treatment of thermal transport composite modeling within the framework of the lattice Boltzmann equation. In the fourth and final section, experimental efforts are presented as a validation of the theoretical ideas presented through two representative studies on how the functionalization of dispersed graphite flakes and anisotropy can enhance the through-thickness thermal conductivity by tailoring the interface thermal resistance. To acquaint our readers with the various modeling approaches used in different sections, we give an overview of each method's background and associated fundamentals, followed by the aforementioned studies at different length scales.

2. THERMAL TRANSPORT CHARACTERIZATION THROUGH ATOMISTIC MODELING

2.1. Brief Overview of Equilibrium Molecular Dynamics (EMD) Simulations. Equilibrium MD, also known as the Green−Kubo (GK) approach, is based on the fluctuation−dissipation theorem and relates the fluctuations in a thermodynamic system to its linear response properties[5] through an autocorrelation function. A few of such examples include the diffusion coefficient, thermal conductivity, electrical conductivity, viscosity, etc. In particular, the thermal conductivity, k, within this formalism, is calculated by integrating the time autocorrelation function of instantaneous heat flux and is given by following equation.

$$k = \frac{1}{3k_B T^2 V}\int_0^\infty \langle \mathbf{J}(t)\mathbf{J}(0)\rangle dt \tag{1}$$

Here, $\mathbf{J}(t)$ is the heat flux vector at time t. In addition, V and T represent the volume and temperature of the system, respectively, whereas k_B is the Boltzmann constant. In terms of the molecular dynamics entities, $\mathbf{J}(t)$ can be written as

$$\mathbf{J}(t) = \frac{d}{dt}\sum_{i=1}^{N} r_i E_i \tag{2}$$

where

$$E_i = \frac{1}{2}m_i v_i^2 + \frac{1}{2}\sum_{j\neq i}^{N} u(r_{ij})$$

Here, m_i and v_i represent the mass and velocity of atom i, $u(r_{ij})$ is the total potential energy of atom i, and r_{ij} is the distance between atom i and j. In most cases, an analytic form of $\mathbf{J}(t)$ is used which generally depend upon the form of interaction potential $u(r_{ij})$ employed in the simulations. In terms of observable molecular variables, the detailed expression for the microscopic heat current vector $\mathbf{J}(t)$ becomes

$$\mathbf{J}(t) = \frac{1}{2}\sum_{i=1}^{N}[m_i v_i^2 + \sum_{j\neq i}^{N} u(r_{ij})]\mathbf{v}_i + \frac{1}{2}\sum_{i=1}^{N}\sum_{j\neq i}^{N}(\mathbf{r}_{ij}\mathbf{F}_{ij}^R)v_i + \frac{1}{2}\sum_{i=1}^{N}\sum_{j=1}^{N}\mathbf{v}_i\vec{\mathbf{S}}_{ij} \tag{3}$$

In the above equation, $\mathbf{F}_{ij}$ represents the short-range van der Waals force and the real part of the Ewald-coulomb force. These forces are computed in real space, whereas tensor $\mathbf{S}$ is evaluated in Fourier space. The elements of tensor $\mathbf{S}$ are written as

$$\mathbf{S}_{ij}^{\alpha\beta} = \frac{4\pi}{V}\sum_{k\neq 0}^{\infty} B_{\alpha\beta}\frac{1}{|k\cdot k|}e^{-k^2/4R_C^2}Z_i Z_j \cos(\mathbf{k}\mathbf{r}_{ij}) \tag{4}$$

$$B_{\alpha\beta} = \delta_{\alpha\beta} - \frac{2|\mathbf{k}_\alpha||\mathbf{k}_\beta|}{|\mathbf{k}|^2} - \frac{|\mathbf{k}_\alpha||\mathbf{k}_\beta|}{2R_C^2} \tag{5}$$

where α and β denote the direction in reciprocal space, $\mathbf{k}$ represents the reciprocal vector, R_C represents an Ewald parameter, and i and j are atom indices. In addition, Z_i denotes the charge on atom i. A detailed discussion for the inclusion of tensor $\mathbf{S}$ in the heat current vector has been reported elsewhere.[6] Here, it is sufficient to say that it is introduced in order to avoid divergences arising from the long-range columbic interactions and takes care of forces due to long-range columbic interactions in Fourier space.

2.2. Brief Overview of Non-Equilibrium Molecular Dynamics (NEMD) Simulations. Nonequilibrium MD simulations provide an alternative approach to estimate thermal conductivity within an MD framework.[7] It is also known as the "direct method" and has its origin in Fourier law of thermal conduction. The thermal conductivity, k, can be estimated as

$$k = \frac{Q/A\Delta t}{dT/dz} \tag{6}$$

Here, $Q/A\Delta t$ is the heat flux through a specified cross-section, A, and dT/dz is the steady-state temperature gradient. Under this formalism, there are two well-known methods used to calculate thermal conductivity, k, termed as constant temperature method and constant heat method. Although the

preparation for the initial condition for performing NEMD simulation is same, they differ in how the heat flux is maintained and evaluated during the course of the simulation. For both approaches, first, the system of interest is created as a long, thin slab along one direction and equilibrated at the desired temperature and pressure. Next, the slab is divided into a predefined number of bins for the temperature profile calculation.

In the constant temperature approach, a few bins (known a priori) in the central region of the slab are thermostatted to the desired temperature, T_{high}, whereas the end boundaries are kept at a relatively low temperature T_{low}, through a separate thermostat. To keep the regions at their specified temperatures, energy is continuously added and removed from the hot and cold region, respectively, during the course of the simulation. Various thermostats, such as Nose-Hoover and temperature rescaling, are often used for temperature control. On the other hand, in the constant heat approach, a constant amount of energy is added and taken off from well separated, predefined bins (also called "hot" and "cold" regions), similar to those discussed above. This is either achieved by adding (removing) given energy (known a priori) to the hot (cold) region, or exchanging velocities of the hottest and coldest atoms in "hot" and "cold" bins. The latter approach is also famously known as the reverse-NEMD approach.[8] Along with energy exchange (Q), its frequency and the cross-sectional area under consideration provide us with the value of the heat flux, $Q/A\Delta t$.

By applying any of the aforementioned methods, a temperature gradient is established across the slab over time. The temperature of each bin within the slab can be calculated as follows.[7]

$$T_i = \frac{1}{3N_i k_B} \sum_{k=1}^{N_i} m_k v_k^2 \tag{7}$$

where, N_i is the number of atoms in the ith slab. Furthermore, the calculated temperature of each slab, T_i, is averaged over several pico-seconds to get a smooth temperature profile. Finally, the temperature gradient is calculated from the slope of the resulting temperature profile. Once the temperature gradient and the heat flux are known, the thermal conductivity is calculated using eq 6.

2.3. Thermal Conductivity of Epoxy Networks from Molecular Modeling. To gain fundamental insights toward mechanisms of thermal conduction in epoxy composites, the thermal conductivity of epoxy networks and their un-cross-linked constitutive elements was modeled using both equilibrium MD and nonequilibrium MD simulations. EPON-862 and DEDTA (epicure-W) were chosen as a representative epoxy and curing agent. Its cross-linked network, comprised of these two components, was also developed from scratch (details are reported elsewhere[9,10]). The CVFF force field[11] was employed as this force-field predicted accurate thermodynamic properties of the cross-linked network structure.

For NEMD simulations, the length of the slab geometry was ~37 nm with a cross-sectional area of ~5.5 nm^2. Here, the constant temperature methodology was employed, in which the T_{high} and T_{low} were kept at 350 and 250 K, respectively. The temperature of the thermostatted bins was controlled using velocity-rescaling criterion. The temperature gradient was calculated by fitting the temperature profile along the slab. Incorporating the heat flux, as calculated from velocity rescaling, the thermal conductivities of DETDA, EPON-862 and their cross-linked network was predicted to be 0.20, 0.21, and 0.30 W/m-K, respectively. Although the experimental values of thermal conductivities of DETDA and uncross-linked EPON-862 were not found it literature, the thermal conductivity of cross-linked epoxy network has been mentioned to be between 0.2 and 0.3 W/m-K.[12]

For equilibrium MD simulations, a cubic cross-linked system was employed with a linear dimension of ~4.5 nm (~7500 atoms). Here, the simulations were run in the NVE ensemble for 4 ns at 300 K and data collection for coordinates, velocities and forces was performed every step (1 fs). Figure 1 shows the

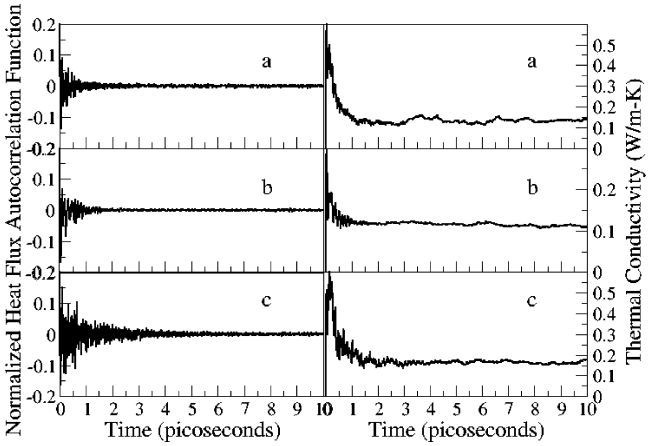

Figure 1. Normalized heat flux autocorrelation function and resultant thermal conductivity values for various studied systems: (a) cross-linked network; (b) EPON-862; (c) cross-linked DETDA.

plot of thermal conductivity as a function of time, as evaluated from integrating the heat flux autocorrelation function. For all cases, the thermal conductivity was found to first increase, then decrease and become constant at longer times when the autocorrelation function decays down to zero. The thermal conductivities for DETDA, EPON-862 and the cross-linked network were calculated to be 0.27, 0.25, and 0.31 W/m-K. Comparing results from equilibrium and nonequilibrium molecular dynamics simulations, a good agreement between both approaches was found. However, the results from EMD simulations were found to be slightly higher than those from NEMD simulations for all cases. Although size effects for NEMD simulations were not considered because of computational limitations, an EMD simulation of the cross-linked network was performed for a system twice as big as the previous system with ~15 000 atoms. The estimated thermal conductivity value was found to be ~0.32 W/m-K, in excellent agreement with the smaller cross-linked system, providing us with sufficient evidence that studied system sizes through EMD simulations were large enough for the estimation of thermal conductivity for the cross-linked system.

The power spectra of the cross-linked network structure was also calculated, as shown in Figure 2, for various atomic entities as partial vibrational density of states (PVDOS). It can be seen that each subfigure has several peaks for each atomic type. The high-frequency peaks represent different vibrations (stretching, bending, etc.) in which the corresponding atomic entity is involved. These high-frequency vibrations in polymeric glasses are known to be hardly involved in thermal transport, as these modes are localized with negligible thermal diffusivity.[13] The figure also presents a broad low-frequency peak that is present for all the atomic entities. Generally, these peaks are associated

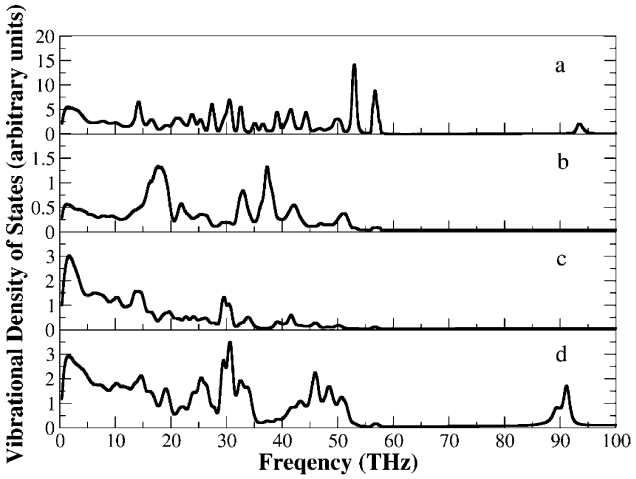

Figure 2. Vibrational density of states for: (a) sp^2 benzene carbon; (b) amine nitrogen; (c) ether and hydroxyl oxygen; and (d) sp^3 carbon in methyl and methylene groups in cured epoxy network.

with low-frequency modes of vibrations, known to be significant for thermal conduction due to their nonzero thermal diffusivity.[13] For the system of interest, one such broad peak was seen, present in the power spectra of all atomic entities. The similar position of the peak for all atomic types suggests that a significant number of different types of atoms are perhaps collectively involved in these low-frequency vibrations. The broadness of the peak over several THz suggests a possible distribution of relaxation times with different overlapping low-frequency vibrational modes. The broad nature of the low-frequency peak can be attributed to the amorphous nature of the studied polymer network system as also observed recently by Shenogin et al.[13]

2.4. Pair Contribution Analysis. Although NEMD simulations predict thermal transport properties in a straightforward manner, equilibrium MD simulations provide many additional details behind the origin of low thermal conductivity, such as the contributions of different types of interactions toward thermal conductivity. Equation 3 shows that the heat flux is indeed comprised of several convective and virial terms. These terms are associated with (a) kinetic energy; (b) van der Waals potential energy; (c) electrostatic potential energy; (d) forces due to van der Waals interactions; (e) forces due to electrostatic interactions (within a certain cutoff, calculated in real space); (f) forces due to long-range electrostatic interactions (outside the cutoff, calculated in Fourier space); (g) bond stretching forces; and (h) angle bending forces. Note that terms a−c are convective, whereas d−h are virial in nature.

To capture different contributions, we evaluated each term in eq 3 separately and stored it at each time step during the course of the simulation. As an example, to evaluate the thermal conductivity due to kinetic and potential energy contributions only, we summed the terms associated with a and b when calculating the heat flux, while ignoring all other terms. The most important findings that emerge from this analysis are presented in the form of pie charts in Figure 3.

Upon careful analysis, the contributions from virial terms were found to have a dominating effect compared to convective terms and are in agreement with previous literature on ionic systems.[14] Moreover, the cross-correlation between convective and virial terms was found to be insignificant. The forces due to van der Waals interactions were found to be the most dominating among the different virial contributions to thermal conductivity while the contributions from the bonded terms are negligible. In addition, the contributions from long-range electrostatic forces to the overall thermal conductivity were also found to be negligible. This suggests that such contributions can be neglected while doing thermal analysis for organic, neutral polymeric systems.

In summary, the aforementioned analysis suggests that the dominant mode of heat transport for disordered amorphous polymeric materials is due to van der Waals interactions and their corresponding forces. These interactions result in anharmonic modes of vibrations, contributing toward a low value of thermal conductivity for polymeric networks. These results are in agreement with a recent study which suggests that anharmonic interactions contribute significantly toward thermal conductivity in polymeric glasses.[13] It is also suggested that in polymeric glasses, a large fraction of vibrational modes (especially high-frequency vibrational modes) are localized with negligible thermal diffusivity. Keeping that in mind, contributions from these vibrational modes toward thermal conductivity are expected to be insignificant. This is also in agreement with the

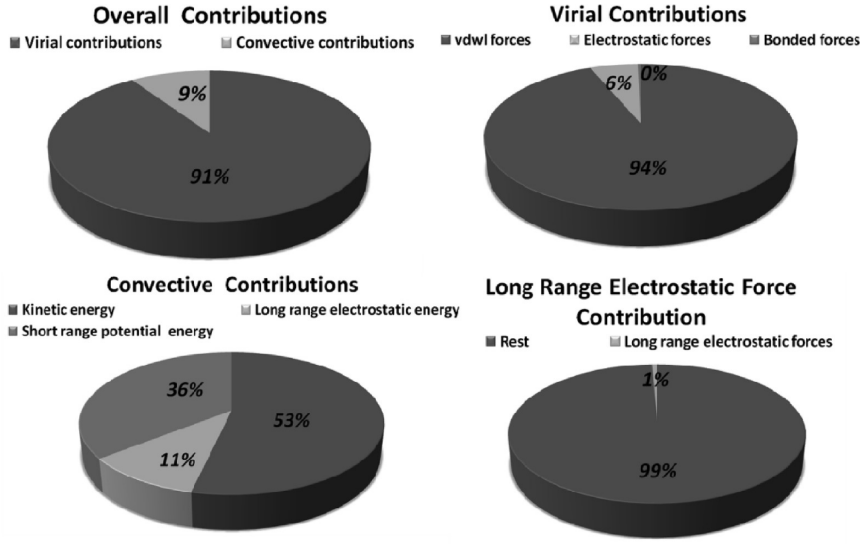

Figure 3. Contribution analysis toward thermal conductivity from different heat flux components.

results where negligible contributions from bonded interactions were found.

2.5. Prediction of Thermal Interface Conductance: Effect of Functionalization. When carbon nanotubes are added as a filler to an epoxy matrix, the resultant nanocomposites show a marginal increase in composite thermal conductivity.[1,2] This is primarily attributed to the thermal resistance at the CNT-matrix interface, also known as Kapitza resistance.[15] Atomistic simulations were performed to determine if this resistance can be modified through functionalization of the nanotubes.

All simulations were performed using the LAMMPS MD package with CVFF force field. For this study, a system was developed within Materials Studio; by randomly placing 512 EPON-862 molecules and 256 DETDA molecules around a (10,0) carbon nanotube. The functionalization of the nanotube with DETDA molecules was performed using the dynamic cross-linking algorithm.[9] The functionalized nanotube and the representative system are shown in Figure 4a. The initial system

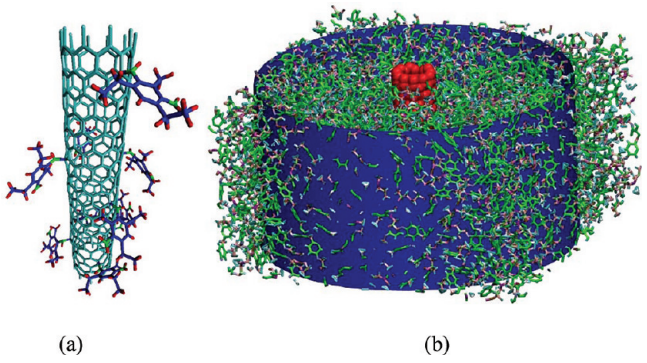

Figure 4. (a) Schematic of a nanotube, functionalized with cross-linker DETDA. (b) Schematic of CNT−epoxy matrix as a heat source and sink system. The CNT (in red) signify the heat source, whereas the outermost blue shell of 3 Å width corresponds to heat sink.

was equilibrated in NVT and NPT ensembles at 300 K and atmospheric pressure for 100 ps with a time step of 1 fs.

To measure interface thermal conductance, we divided each system into 12 concentric cylindrical shells of equal width (3 Å) with the nanotube at the center. Here, constant energy at the rate of ~5×10^{-8} J/s was added at the source (CNT) with the same amount removed at the sink (outermost shell) as shown in Figure 4b, thus creating a radial temperature gradient. The average temperature for each cylindrical shell was then calculated using eq 7. The Kapitza conductance was then estimated from the applied heat flux and the temperature drop at the CNT−matrix interface.

The radial temperature profiles for each system as a function of CNT functionalization (up to 2.5%) is plotted in Figure 5a. The analysis of the plot reveals a sharp discontinuity at the nanotube-matrix interface. Although the error bars associated with steady-state bin temperatures are significant, it is clear that there is a specific trend in ΔT with respect to CNT functionalization. For a constant value of thermal in/out flux (~5×10^{-8} J/s), the plot shows that CNT functionalization leads to the reduction in temperature discontinuity or higher thermal energy transfer between the transverse CNT walls and the matrix. The resulting Kapitza conductance (interface thermal conductance) is plotted in Figure 5b.

The results for unfunctionalized as well as functionalized (0.77−2.5 × 10^{-8} m^2-K/W) CNT interface boundary resistance are in excellent agreement with previously reported values in experiments as well as simulations.[16] After fitting the conductance data with the least-squares method, the Kaptiza conductance was found to follow a linear increase with the degree of functionalization up to 2.5% CNT functionalization. The current study clearly shows that functionalization of CNTs increases the thermal transfer between highly conductive nanotubes and the surrounding matrix. Effective composite thermal conductivity depends—in addition to the interface thermal resistance—on the conductivity of the nanofillers such as CNTs. Although the functionalization of CNTs increases the conductance at the interface by providing additional channels for thermal transport, it also introduces defects in high thermally conductive CNTs. These defects act as scattering points for coherent vibrations along the nanotube and reduce overall conductivity of the CNTs significantly. Hence, the functionalization of CNTs is expected to result in two competing effects, i.e., increased interface conductance and reduced filler conductivity, which eventually determine the effective system-level thermal conductivity of the composite material.

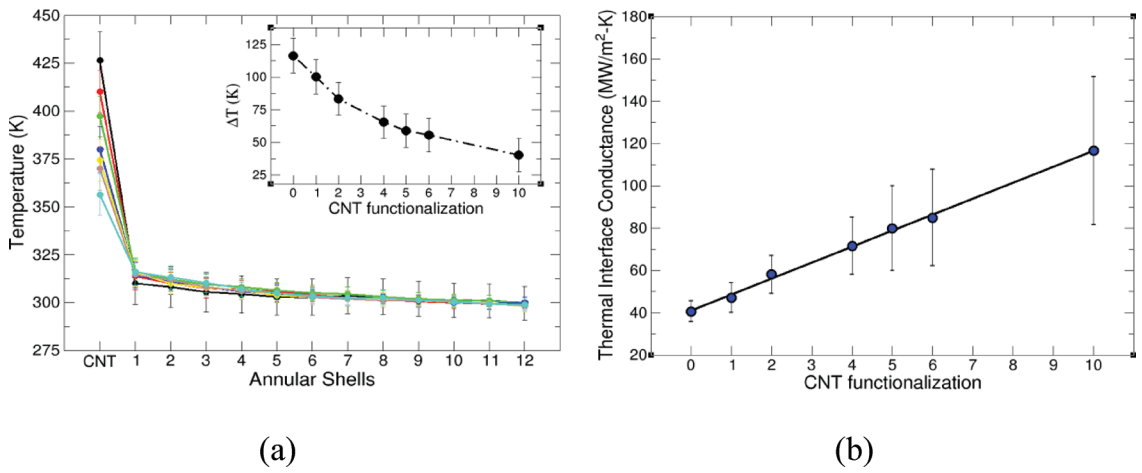

Figure 5. (a) Radial distribution of system temperature in steady state conditions for several degree of CNT-functionalization for epoxy matrix. Color scheme: black (0), red (1), green (2), blue (4), yellow (5), brown (6), turquoise (10). Inset: Temperature drop at the CNT−matrix interface vs degree of functionalization. (b) Interface thermal conductance for several degree of CNT functionalization.

dx.doi.org/10.1021/am201496z | ACS Appl. Mater. Interfaces 2012, 4, 545−563

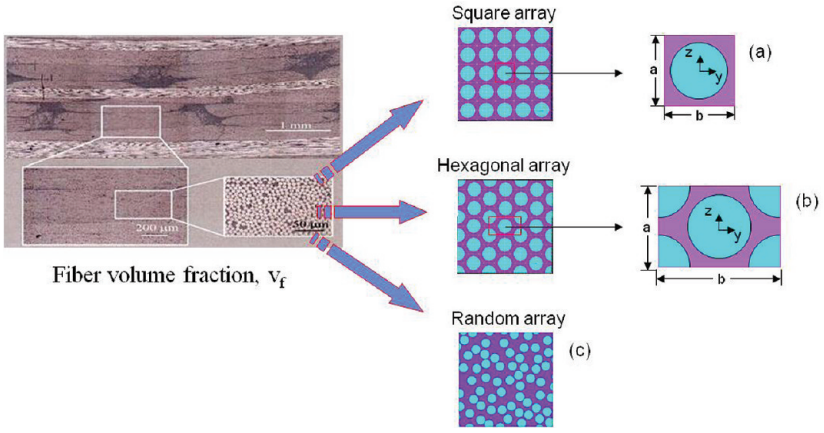

Figure 6. Schematic of micromechanical modeling for prediction of thermal properties of fiber-reinforced composites.[41]

3. MICROMECHANICAL ANALYSIS FOR THE PREDICTION OF EFFECTIVE THERMAL CONDUCTIVITY OF COMPOSITES

In the previous section, the effect of fillers, such as CNTs, in the polymer matrix on the thermal transport characteristics was reviewed toward modifying thermal properties of the matrix phase in composites. In addition to the modified matrix phase, traditional fiber reinforcements in composites also influence its thermal properties. This section reviews analytical and numerical studies for the prediction of effective thermal conductivities of fiber-reinforced composite materials using continuum-based micromechanical approaches. This micromechanical analysis discretely models fiber and matrix constituents in the composites as well as their interfacial thermal resistance. Figure 6 shows a schematic of the micromechanical modeling used for the calculation of the effective thermal conductivities of composites. A cross-section of composites is typically modeled with idealized regularly distributed arrays of fibers in either square or hexagonal patterns, and the model can further be simplified to a representative unitcell model as a repeating block. Alternatively, randomly distributed fibers can be simulated with the random array model, whose fiber distributions can be obtained by either optical microscopic measurements or computer simulations using random number generators. The micromechanical models commonly make assumptions that fiber and matrix constituents are homogeneous and isotropic materials (c.f., transversely isotropic for carbon fiber), and the composites are macroscopically homogeneous. The effective thermal properties of the composites are then obtained by smearing the constituents' properties. It is well-known that the composite properties, especially thermal conductivity, are significantly influenced by additional parameters such as void contents and imperfect interfaces between the fiber and matrix constituents.

Several analytical approaches have been developed to predict the effective thermal conductivity of composites. Among them, simple analytical solutions based on rule-of-mixture (ROM) methods are widely adopted in the thermal property calculation. Longitudinal and transverse thermal conductivities of the transversely isotropic fiber are denoted as k_{1f} and k_{2f}, respectively, and that of the isotropic matrix as k_m. With respect to an orientation of the transversely isotropic fiber, two different effective thermal conductivities can be obtained in the directions parallel and perpendicular to the longitudinal direction of the fiber, which are denoted as effective longitudinal (k_x) and transverse (k_z) thermal conductivities, respectively. Simple rule-of-mixture (SROM) solutions for k_x and k_z can be derived by an electrical resistance analogy based on a parallel (Voigt) and a serial (Reuss) models, respectively, as

$$\text{SROM: } k_x = v_f k_{2f} + (1 - v_f)k_m \quad \text{and} \quad \frac{1}{k_z} = \frac{v_f}{k_{2f}} + \frac{1 - v_f}{k_m} \tag{8}$$

where v_f is a volume fraction of the fiber. The SROM yields a sufficiently accurate solution for k_x. However, the accuracy of the SROM solution for k_z is questionable because effects of geometric shape and arrangement of the fibers in the composites are not considered, especially in the case of two-dimensional heat flow when the conductivities of fiber and matrix are orders-of-magnitude different.

More refined models have been derived as the enhanced rule-of-mixture (EROM) by considering more realistic shapes of the fiber, such as square and circle. Springer and Tsai[17] developed the unitcell model for the square-array fiber distribution with square- and circular-shaped cross-sections of fiber. The solution was obtained by dividing the unitcell domain into several subdomains, and applying the ROM using a combination of serial (Reuss) and parallel (Voigt) models. Chamis[18] provided the same analytical solution as Springer and Tsai using the square-array unitcell model for square-shaped fiber. The EROM solutions of k_z for square- and circular-shaped fibers can be written as[17,19]

$$\text{EROM (square-shaped fiber): } \frac{k_z}{k_m} = \frac{\sqrt{v_f}}{\sqrt{v_f}/\beta + 1 - \sqrt{v_f}} + (1 - \sqrt{v_f}) \tag{9}$$

dx.doi.org/10.1021/am201496z | ACS Appl. Mater. Interfaces 2012, 4, 545–563

EROM (circular-shaped fiber):

$$\begin{cases} \dfrac{k_z}{k_m} = 1 - \dfrac{1}{c} + \dfrac{\pi}{2d} - \dfrac{2c}{d\sqrt{c^2 - d^2}} \tan^{-1}\dfrac{\sqrt{c^2 - d^2}}{c + d} & \text{for } c^2 > d^2 \\ \dfrac{k_z}{k_m} = 1 - \dfrac{1}{c} + \dfrac{\pi}{2d} - \dfrac{c}{d\sqrt{d^2 - c^2}} \ln\dfrac{d + \sqrt{d^2 - c^2}}{c} & \text{for } c^2 < d^2 \end{cases} \quad (10)$$

where $\beta = k_{2f}/k_m$, $c = (\pi/v_f)^{1/2}/2$, and $d = 1/\beta - 1$. Zhou et al.[19] derived another analytical expression for the transverse thermal conductivity of the unidirectional composites with a consideration of the interfacial thermal resistance between the fiber and matrix phases. The EROM with more realistic fiber shapes can certainly offer a more accurate solution for k_z than the SROM solution, especially when the thermal conductivities of fiber and matrix are vastly different.

Benveniste et al.[20−26] developed explicit expressions for the effective transverse thermal conductivity of the composites using a self-consistent scheme and a Mori−Tanaka mean-field method.[27] They considered various shapes of conducting phase of materials including particulate, ellipsoidal, infinitely long fiber, etc., with the presence of interfacial coating and microvoids/cracks. Hatta and Taya[28−30] proposed a similar approach based on an equivalent inclusion method (EIM) to analytically calculate the effective thermal conductivity of composites having aligned or misoriented fibers with and without the presence of the interfacial coated layer. The EIM is analogous to an Eshelby's equivalent inclusion method in elasticity.[31] The EIM takes into account interactions among the fibers of various orientations. Particularly, the EIM analytical solution for k_z of the aligned infinitely long circular fiber can be written as

$$\text{EIM: } \frac{k_z}{k_m} = \frac{(\beta + 1) + v_f(\beta - 1)}{(\beta + 1) - v_f(\beta - 1)} \quad (11)$$

Note that eq 11 can also be derived by a self-consistent model based on Rayleigh's potential theory.[32] Nan et al.[33] used the EIM to predict the effective thermal conductivity of arbitrary particulate composites with interfacial thermal resistance with a concept of Kapitza thermal contact resistance. Results compared well with existing analytical models and available experimental results for particulate-reinforced diamond/ZnS, diamond/cordierite, and SiC/Al composites. The EIM approach was also used by Nan and Lin[34] to predict the effective thermal conductivity of the nanotube-based composites.

The transverse thermal conductivity of composites appears to be sensitive to their microstructure morphology, such as ordered vs randomly distributed fiber spacing, etc., which may not be readily incorporated in the analytical models. Meanwhile, the numerical models can offer the flexibility of incorporating more realistic microstructure morphology. Among several numerical analyses, Islam and Pramila[35] conducted a finite element (FE) analysis to calculate the effective through-thickness conductivity of the composites having the square-array pattern of fibers. They studied the high and low ratios of the thermal conductivities between fiber and matrix constituents, along with the effect of the imperfect interface between the fiber and matrix using the FE analysis. In addition, Noor and Shah[36] used the square and the hexagonal FE models to assess the accuracy of the thermoelastic and thermal properties of unidirectional fiber-reinforced composites predicted by several analytical models including the self-consistent model[37] and the EIM. The comparison of the analytical and numerical FE predictions of the transverse thermal conductivity with experimental data for four different composite material systems (two types of graphite fiber/epoxy matrix, silicon carbide fiber/glass ceramic matrix and silicon carbide fiber/epoxy matrix) reveals that the predictions by the EIM are in very good agreement with those obtained by the hexagonal FE model compared with other analytical models considered. Rolfes and Hammerschmidt[32] conducted analytical, numerical and experimental studies on the transverse thermal conductivity of the laminated composites. They considered four analytical formulas including the solutions obtained by a Rayleigh's potential theory[38] and the self-consistent model. The numerical calculations carried out by the FE method on the square- and hexagonal-array unitcell models show good agreement with Rayleigh's potential theory and self-consistent model, respectively, for volume fractions ranging from 0.4 to 0.7. They also concluded, from the comparison of the two analytical solutions and their experimental measurement, that the self-consistent formula fits the experimental data better than the Rayleigh's model if corrected by void content. Duschlbauer et al.[39] conducted numerical FE simulations for the thermal conductivity of metal matrix composites with aligned continuous and aligned short fibers with the consideration of the thermal barrier at the interface of fiber and matrix constituents. They modeled the square- and hexagonal-array unitcells as well as a random multicell consisting of 60 fibers. They used a contact element for the thermal barrier interface without discretely modeling the third phase elements, ranging from perfectly insulating interfaces to perfectly conducting interfaces. Al-Nassar[40] used the FE analysis to predict the thermal conductivity of microvoided composites.

Sihn and Roy[41] recently revisited and investigated the accuracy and validity of the various micromechanical models for the calculation of the effective thermal conductivity of laminated composites. The numerical FE models of the unitcells with the regular square- and hexagonal-array patterns of fibers as well as randomly distributed fibers were used to compare these numerical solutions with the analytical ones using the EROM and EIM for wide ranges of fiber volume fractions and fiber-to-matrix conductivity ratios. This study was conducted with assumptions that the composites are void-free and the interfacial resistance between the fiber and matrix is negligible. Uniform temperature boundary conditions were applied on the top and bottom sides of the unitcell, whereas periodic boundary conditions were applied on the vertical sides of the unitcell. Figure 7a shows the numerical FE and analytical solutions for the k_z normalized by k_m with respect to various values of v_f. The FE solutions for the square- and the hexagonal-array models agree well with each other for $v_f < 0.5$. The square-array model yields significantly higher k_z than the hexagonal one for higher v_f, especially when the fiber periphery is close to the unitcell boundaries. The analytical solutions by the SROM and the square-shape EROM underestimate the k_z significantly. Although the square-shape EROM is based on the square-array unitcell, the k_z values are closer to the hexagonal-array FEM solution. While the circular-shaped EROM agrees well

dx.doi.org/10.1021/am201496z | ACS Appl. Mater. Interfaces 2012, 4, 545−563

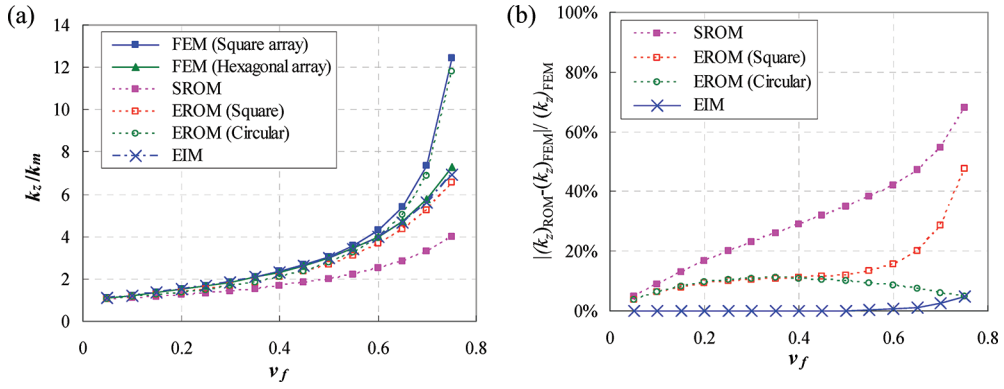

Figure 7. (a) Normalized through-thickness thermal conductivity (k_z/k_m) of composites predicted by various numerical and analytical methods and (b) difference between numerical and analytical solutions against various volume fractions of fiber (v_f).[41]

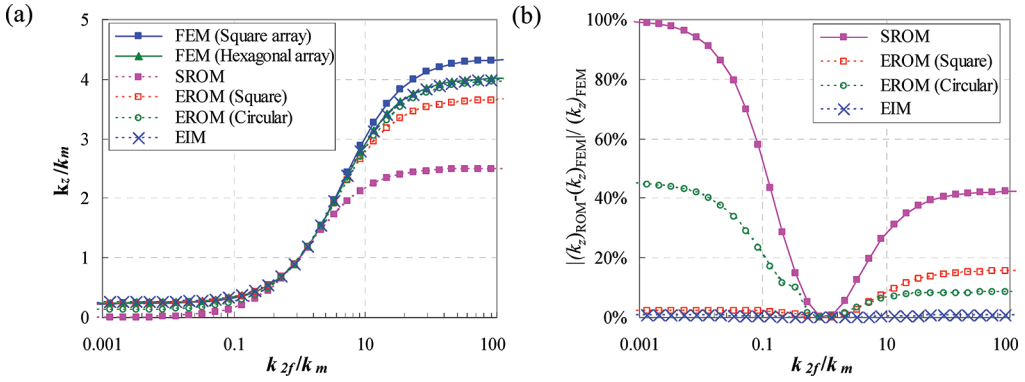

Figure 8. (a) Normalized through-thickness thermal conductivity (k_z/k_m) of composites predicted by various numerical and analytical methods and (b) difference between numerical and analytical solutions against various ratios of thermal conductivities of fiber and matrix constituents (k_{2f}/k_m).[41]

with the square-array FE model, the EIM analytical solution agrees well with the hexagonal-array FE solution. Therefore, the random distribution of fibers, which is implicitly considered by the EIM, can be represented well by the hexagonal FE model. Figure 7b plots the difference between the analytical and FE solutions. The SROM and two EROM solutions are compared with the square-array FE one, whereas the EIM solution is compared with the hexagonal-array FE result. Both the circular-shaped EROM and the EIM yield less than a 12% difference between the numerical and analytical solutions for $0 < v_f < 0.75$, whereas the SROM and the square-shaped EROM yield a significant difference, especially at high v_f. Figure 8a shows the numerical FE and analytical solutions for the k_z normalized by k_m against the variation of thermal conductivity ratios of fiber and matrix constituents, k_{2f}/k_m, at $v_f = 0.6$, and Figure 8b shows the difference between them. For a wide range of k_{2f}/k_m ratios, the same trend was observed as before. Note that the circular-shaped EROM yields a significantly different solution from the square-array FE solution for small k_{2f}/k_m. The EIM yields nearly identical results with the hexagonal-array FE solution for all k_{2f}/k_m ratios.

To study the effect of the irregularity of the fiber distribution on the transverse thermal conductivity of composites, Sihn and Roy[41] also developed a random fiber model by generating several fibers of same diameter in random locations in a square box. Random-fiber results were compared with the numerical and analytical solutions using the regular fiber array models. The number of fibers in the square cell was determined by the corresponding fiber volume fraction, which can be determined by the ratio of the total circular cross-sectional area of all fibers to the area of the square cell. Direct contacts among the fibers were avoided by allowing a small gap between adjacent fibers to prevent difficulties in generating the FE meshes. In this study, the gap was set as 1.1% of the radius of the circular fiber. Two scenarios were considered: (i) fibers inside box: the whole portions of all fibers are located inside the square box, and no fiber is located across the cell boundary; (ii) fibers outside box: portions of the fibers are allowed to cross the square boundary. In the latter case, the fibers across the boundaries were cut along the boundaries, and only the portions of the fibers within the square cell are considered for the analysis. Because the fiber locations near the boundaries are less restricted, a higher maximum packing density of the fibers can be achieved with the latter case (ii) than with the former one (i). Five realizations of the randomization for the fiber locations were generated for each volume fraction using a random number generator built in Microsoft Excel. Uniform temperature boundary conditions were applied to the top and bottom sides of the square box, while adiabatic boundary conditions were applied to the vertical sides. Figure 9 shows the normalized k_z values predicted by the random fiber model against the variation of v_f at the fiber-to-matrix thermal conductivity ratio of $k_{2f}/k_m = 666$ along with temperature distributions for several values of v_f. Results from the two scenarios of the fiber confinement in the square cell are plotted with triangular and circular markers, respectively. For comparison, the results of the unitcell models with the regular square- and hexagonal-arrays of fibers are also plotted with dotted lines as well as the experimental data measured by Thomburg and Pears[42] with a cross marker. Figure 10 shows the differences of k_z between the random fiber prediction and

dx.doi.org/10.1021/am201496z | ACS Appl. Mater. Interfaces 2012, 4, 545–563

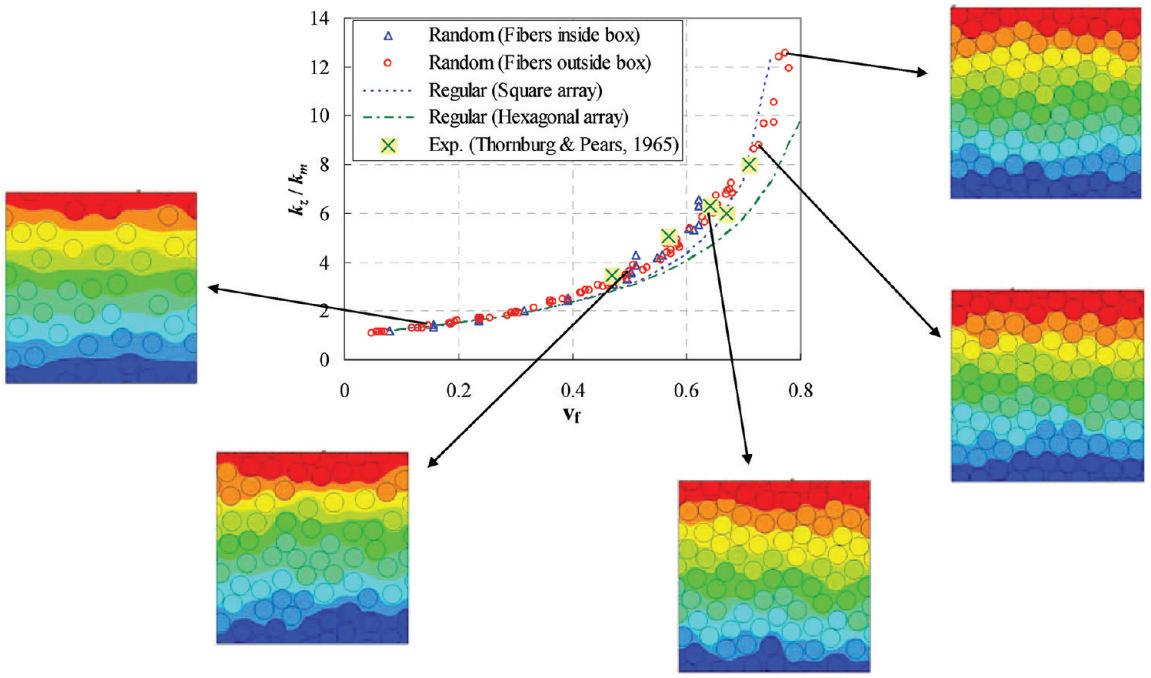

Figure 9. Normalized transverse thermal conductivity (k_z/k_m) of composites with randomly distributed fibers against volume fractions of fiber (v_f).[41]

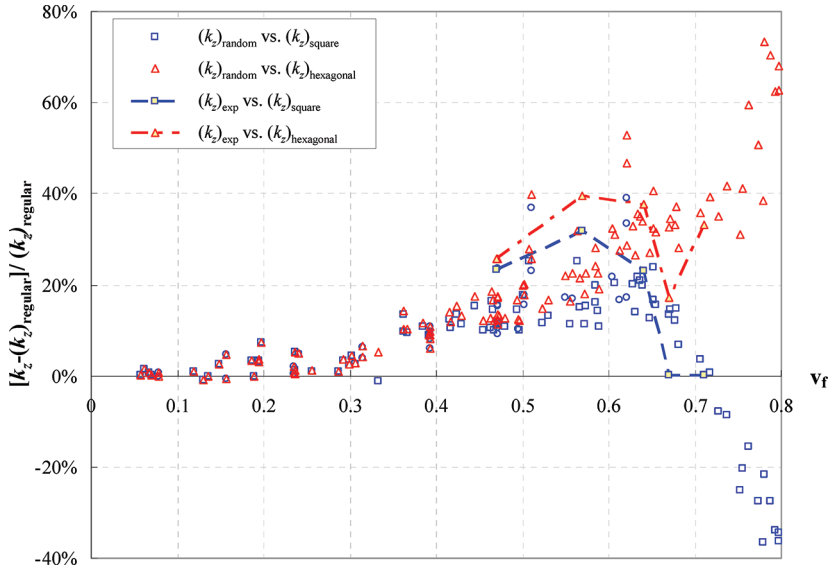

Figure 10. Difference of predicted transverse thermal conductivity of composites between random- and regular-fiber models against volume fractions of fiber (v_f).[41]

the regular fiber one at each v_f. In this figure, the differences were normalized by the regular fiber solutions with square ($(k_z)_{square}$) and hexagonal ($(k_z)_{hexagonal}$) arrays, and plotted with square and triangular markers, respectively. Figure 10 also shows a comparison of the difference between the experimental data and two regular fiber solutions in dotted lines. From both Figures 9 and 10, for the wide range of v_f, the following observations were made.

For low v_f (<0.4), both fiber packing scenarios (inside and outside box) agree well with each other because of the sparcity of the fibers. For higher v_f, the case with the fibers inside the box tends to yield slightly higher k_z than the case with the fibers outside the box. However, the overall trend is similar to each other for the wide range of v_f. For v_f < 0.3, the random fiber solutions agree well with the regular fiber ones. However, for higher v_f, the random fiber solutions consistently yield higher k_z than both regular fiber cases up to 70% of v_f, which is a practical upper bound of the fiber packing density in composites. The difference between the random and the regular fiber solutions can be more than 20% near v_f = 0.6. For even higher v_f (>0.7), the random fiber solutions lie between the two regular fiber ones, following the trend of the square-array unitcell model more closely. Therefore, the transverse thermal conductivity of composites with real irregular fiber distributions can be significantly different from that predicted by the idealized unitcell models with regular fiber array distributions. Figure 10 indicates that the experimental data are significantly higher than both regular fiber solutions for v_f < 0.65, and then follow the

dx.doi.org/10.1021/am201496z | ACS Appl. Mater. Interfaces 2012, 4, 545–563

trend of the square-array FE solution for higher v_f. It was concluded that, although there might still be other reasons, the under-prediction of the experimental data compared with the unitcell model predictions can be explained with the effect of the random fiber distribution.

4. MESOSCOPIC THERMAL COMPOSITE MODELING

As discussed in the previous section, the effective thermal conductivity of the composite materials in the macroscale is a well-defined boundary value diffusion problem. The geometric location of boundaries between the matrix and filler phases, along with the thermal conductivity of each material phase, determines the effective thermal property of the composite. As the system size decreases, two distinct features, which are irrelevant and negligible at the macroscale, gradually emerge. One of them regards the resistance of the system to the heat flow. The total resistance of the system to the heat flux comes from the bulk materials, either the matrix or the filler, and also from the interface between them. Although the interface thermal resistance can usually be neglected in large-scale systems, the enhanced surface-to-volume ratio in the small-scale system, especially for nanoscale devices, allots a significant portion of the total resistance to the interface. The magnitude of the interface resistance can be conveniently represented with a length scale named the Kapitza length.[43] The Kapitza length of η means that the magnitude of the interface resistance to the heat flux is comparable to the resistance coming from the bulk of the material whose thickness is η. For a composite material, the interface resistance can be neglected only when both the interparticle separation distance and filler size are much larger than the Kapitza length.

The other additional feature regards the very definition of thermal conductivity. Traditionally, the thermal modeling in the engineering scale relied on the heat diffusion with a well-defined thermal conductivity. However, as either the interparticle distance or the filler size decreases close to the mean free path of the energy carrier, the thermal conductivity becomes dependent on the size and shape of the boundary and ceases to be a material property. This size and shape dependence of the thermal conductivity is associated with the finiteness of the Kundson number which is defined as the ratio of the carrier mean free path to a representative system length-scale.

When the system size is small enough so that the Kapitza length and the carrier mean free path must be considered, but still too large for a microscopic simulation involving atomistic degrees of freedom, a mesoscopic modeling strategy is required. The Boltzmann kinetic equation has long been the favored choice, because the formalism relies on the carrier distribution function, whose well established coarse graining procedure links the carrier microdynamics with the macroscopic hydrodynamics.[44−46] In this section, the Kapitza length and the finite Knudson number are realized numerically using the mesoscopic lattice Boltzmann Peierls Callaway (LBPC) equation for multiphase phonon gas.[47−49]

First, the core machinery of the LBPC equation is reviewed. Guyer was the first, adopting the lattice Boltzmann scheme to the Boltzmann Peierls Callaway phonon kinetic equation, to propose the LBPC equation,[47]

$$n_i^{\sigma}\left(\mathbf{r} + \frac{v_g^{\sigma}}{c_0}\mathbf{c}_i\delta t,\, t + \delta t\right) = n_i^{\sigma}(\mathbf{r},\, t) + \Delta_i(\mathbf{r},\, t) \tag{12}$$

Here, n_i^{σ} is the probability density function of the phonon with the polarization σ and momentum $p\mathbf{c}_i$, where p is a free parameter to convert the lattice unit of momentum to the real unit of phonon crystal momentum, and $\mathbf{c}_i$ is the velocity vector connecting the lattice node at $\mathbf{r}$ with the neighboring node at $\mathbf{r} + \mathbf{c}_i\delta t$. In a specific LB model, the physical coordinate space and the momentum space are discretized coherently by the set of finite number of velocity vectors, $\mathbf{c}_i$. Regarding features dependent on the specifics of the LB model, refer to references.[46−48] c_0 is the unit speed of LB model; $c_0 = \delta x/\delta t$, where δx is the lattice spacing and δt is the discrete time-step used to update the distribution function. $\Delta_i(\mathbf{r},t)$ is the Callaway collision operator,[50]

$$\Delta_i = \delta t\left(\frac{n_{i,\mathrm{N}}^{\sigma,\mathrm{eq}} - n_i^{\sigma}}{\tau_{\mathrm{N}}} + \frac{n_{i,\mathrm{U}}^{\sigma,\mathrm{eq}} - n_i^{\sigma}}{\tau_{\mathrm{U}}}\right) \tag{13}$$

where $n_{i,\mathrm{N}}^{\sigma,\mathrm{eq}}$ and $n_{i,\mathrm{U}}^{\sigma,\mathrm{eq}}$ are the local displaced Planck distribution and the local Planck distribution of phonons respectively, toward which non-equilibrium n_i^{σ} linearly relaxes with time parameters τ_{U} and τ_{N}. A discussion on the functionality of local equilibrium distributions will follow in the next paragraph. Here, an important feature to mention is that the spatiotemporal scale of the model is determined by the collision operator. The Callaway collision operator does not treat the collision event with any microscopic rigor, but regards the whole phonon collision process collectively as a mechanism to restore the local equilibrium phonon distributions. The mesoscopic character of the LBPC model is due to this coarse-grained description of the phonon collision process. To shorten the discussion of the model and steer the focus swiftly to the Kapitza length and the phonon mean free path, further discussion on the local equilibrium distributions will be based on a simplified model with assumptions of a single polarization and $v_g^{\sigma} = c$. An extended formalism for multipolarization and multigroup velocity can be found elsewhere.[49]

At the ambient temperature of T_0 and the zero phonon drift velocity, $\mathbf{u}_0 = 0$, a strict global equilibrium establishes the Planck distribution of phonons on all lattice sites

$$n_i^{\mathrm{geq}}[\beta_0(t,\, \mathbf{r})] = \frac{w_i}{\exp(\beta_0\varepsilon_i) - 1} \tag{14}$$

Here, ε_i is the phonon energy and $\beta_0 = 1/k_{\mathrm{b}}T_0$, where k_{b} is the Boltzmann constant. w_i is the weight factor depending on the specific LB model to ensure the isotropy of the fourth-order lattice tensor. In the LB model, the local equilibrium distribution is given by the linear perturbation of the global equilibrium distribution subject to the local disturbances in the macroscopic collision invariants, which depends on the specific nature of the collision. The Callaway operator considers two types of phonon collision processes. One is the energy conserving but momentum destroying Umklapp process, through which the nonequilibrium phonon distribution reaches the Planck distribution. The other is the normal collision process conserving both the total energy and the total crystal momentum, through which the phonon distribution restores the displaced Planck distribution. If a local node at $(\mathbf{r},t)$ is subject to the disturbance of temperature $\theta(\mathbf{r},t) = (T(\mathbf{r},t) - T_0)/T_0$ and the phonon drift velocity $\tilde{\mathbf{u}}(\mathbf{r},t) = (\mathbf{u}(\mathbf{r},t) - \mathbf{u}_0)/v_g$ from T_0 and $\mathbf{u}_0$, then the local equilibrium distribution at $(\mathbf{r},t)$ can be approximated to the first order of the linear expansion of the global equilibrium as

$$n_{i,\mathrm{U}}^{\mathrm{eq}} = w_i(A_i - \beta_0\varepsilon_i B_i\theta) \tag{15}$$

dx.doi.org/10.1021/am201496z | ACS Appl. Mater. Interfaces 2012, 4, 545−563

and

$$n_{i,N}^{eq} = w_i(A_i - \beta_0\varepsilon_i B_i\theta - \beta_0\varepsilon B_i \mathbf{c}_i\tilde{\mathbf{u}}) \quad (16)$$

where $A_i = 1/(\exp(\beta_0\varepsilon_i) - 1)$, $B_i = \partial A_i/\partial(\beta_0\varepsilon_i) = -A_i(1+A_i)$, and $\varepsilon = pv_g$. $\theta(\mathbf{r},t)$ and $\tilde{\mathbf{u}}(\mathbf{r},t)$ must be known prior to the collision step to determine local equilibrium distributions, for which the conservation laws for the collision invariants are utilized. The macroscopic energy, E, and the momentum, $\mathbf{P}$, are moments of the phonon distribution function and collision invariants of the Umklapp and the normal processes, respectively. The energy conservation of the Umklapp process,

$$E(t, \mathbf{r}) = \sum_i \varepsilon_i n_i(t, \mathbf{r}) = \sum_i \varepsilon_i n_{i,U}^{eq}(t, \mathbf{r}) \quad (17)$$

has $\theta(t,\mathbf{r})$ as the only unknown. Once $\theta(t,\mathbf{r})$ is determined from energy conservation, the momentum conservation of the normal collision process determines the local drift velocity $\tilde{\mathbf{u}}(\mathbf{r},t)$;

$$P(t, \mathbf{r}) = \sum_i \mathbf{p}_i n_i(t, \mathbf{r}) = \sum_i \mathbf{p}_i n_{i,N}^{eq}(t, \mathbf{r}) \quad (18)$$

Other macro-observables such as heat flux can be calculated as the higher moments of the distribution function.

4.1. Phonon Mean Free Path. A convenient definition of the phonon mean free path in the Callaway collision operator is the distance a phonon travels during the linear relaxation time for the Umklapp collision process; $\Lambda_U = v_g\tau_U$. It refers to the screening length over which the autocorrelation of the phonon momentum decreases exponentially due to the momentum destroying Umklapp process. In typical numerical models including the LBPC equation, however, the time domain is usually discretized by δt; therefore, the definition of Λ_U as the momentum screening length is valid only when $\tau_U/\delta t$ is large. This delicate issue becomes clear in the case where $\tau_U = \delta t$. In the continuous Boltzmann Peierls Callaway formalism, the local phonon distribution exponentially relaxes to the local equilibrium distribution in the finite time scale of τ_U. However, in LBPC formalism, because δt is the time unit of the LBPC equation, τ_U of δt implies an immediate and complete relaxation of phonon momentum and therefore zero mean free path.

An alternative definition of the phonon mean free path, physically meaningful even at small $\tau_U/\delta t$, can be derived from the indirect measurement of the phonon momentum screening length in the LBPC model. The thermal conductivity, k, is a material property definable in the limit of small Knudson number, $Kn = \Lambda/L$, where L is the characteristic size of the material sample. For a homogeneous system with a fixed τ_U, as k was measured for various L, it would increase with L and converge to k_∞ asymptotically at large enough L. If the autocorrelation of the phonon momentum decays exponentially, so that the screening length can be defined, then the thermal conductivity of the homogeneous system can be approximated as

$$k = \frac{k_\infty L}{L + \Lambda_{eff}} \quad (19)$$

where Λ_{eff} is the effective phonon mean free path. When $L \gg \Lambda_{eff}$, k asymptotically converges to k_∞, the material property of the sample. In the other limit of $L \ll \Lambda_{eff}$, k is proportional to L, as expected in the phonon dynamics without Umklapp collision. Therefore, Λ_{eff} can be deduced from a series of k measurements in the system with a fixed τ_U and varying L. The measurement of k is performed in the following procedure. For a given system of a fixed τ_U, a finite temperature difference is applied on two opposite faces separated by L using a Planck distribution. k is given when the measured heat flux is divided by the temperature gradient. Figure 11 compares Λ_{eff}, thus calculated, with Λ_U for a wide range of τ_U. At large $\tau_U/\delta t$, Λ_U is a valid definition of the phonon mean free path within the LBPC model, quantitatively agreeing with Λ_{eff}. However, as $\tau_U/\delta t$ decreases, Λ_U overestimates the actual momentum screening length. Λ_{eff} disappears to zero when $\tau_U = \delta t$.

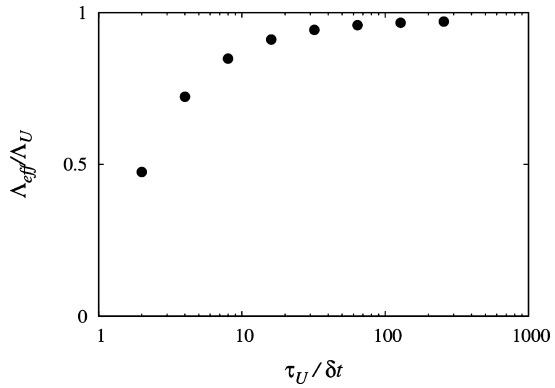

Figure 11. The effective phonon mean free path is plotted against the Umklapp process relaxation time.

4.2. Interface Thermal Resistance. The existence of an interface between the matrix and the filler results in a finite resistance to the heat flux, which is signified by a finite drop in the steady state temperature profile across the interface. The interface thermal resistance ρ is defined phenomenologically as

$$\rho = \frac{\Delta\theta_I}{Q} = \frac{\eta_{m,f}}{k_{m,f}} \quad (20)$$

where $\Delta\theta_I$ and Q are the temperature drop and the heat flux across the interface, respectively. $k_{m,f}$ is the thermal conductivity of either matrix or filler. $\eta_{m,f}$ is the interface Kapitza length based on the thermal conductivity of either matrix or filler. An important fact to be reminded is that, among those parameters associated with the interface, ρ and $\eta_{m,f}$ are local properties of the interface. $\Delta\theta_I$ and Q depend on global conditions, such as the location of the interface and the surface-to-volume ratio of the total system. Because the Boltzmann kinetic equation works on the distribution function, not on phenomenological parameters, the LBPC equation requires a scheme to indirectly control ρ via phonon distribution functions.

In the recently proposed LBPC model for multiphase phonon gas,[49] following the spirit of the Callaway operator for bulk phonon collisions, the interface phonon collision is treated as a linear relaxation process of the phonon distribution function toward a pseudoequilibrium distribution, which is uniquely determined by the collision invariant. Because the interface phonon collision is an Umklapp process, the ansatz of the surface equilibrium distribution follows the Planck distribution, $n_{i,U}^{pep} = w_i(A_i - \beta_0\varepsilon_i B_i\theta^{eff})$, where θ^{eff} is the effective interface temperature, which is used as a numerical variable to satisfy the energy conservation principle, not as a physical interface temperature which is poorly defined. Along with $n_{i,U}^{pep}$, a linear relaxation time parameter τ_I is associated with the phonon interface collision process. As shown in Figure 12, it turns out that ρ and $\eta_{m,f}$ as the local parameters of the thermal

dx.doi.org/10.1021/am201496z | ACS Appl. Mater. Interfaces 2012, 4, 545–563

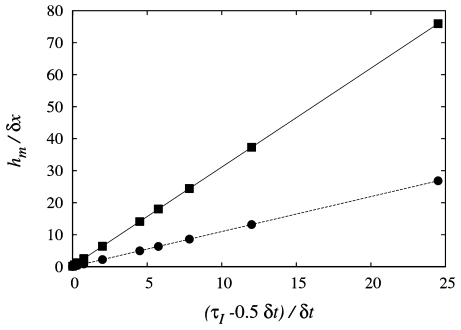

Figure 12. Kapitza length based on the matrix conductivity is plotted against the interface phonon collision relaxation time. Solid squares are for the case where the filler material has a heat capacity that is 30 times larger than that of the matrix. Solid circles are for the case where the phonon mean free path of the filler is 30 δx. To realize the interface of a given thermal resistance, different values of the relaxation time should be used for different filler materials.

interface are linearly proportional to τ_I, which is the only free parameter of the phonon interface collision.

So far, how to realize the interface thermal resistance and the finite phonon mean free path in the LBPC equation has been discussed. Both were interpreted and realized as features of the relaxation process of the nonequilibrium phonon distribution to the local equilibrium. The finite durations, τ_U and τ_I, of the relaxation processes result in the finite phonon mean free path in the bulk phonon dynamics and the finite Kapitza length in the interface phonon dynamics. The LBPC equation finds applications in the large-scale thermal modeling of systems, where mesoscale effects must be considered, such as nanocomposite materials where the phonon mean free path is finite compared to the filler size and the interface resistance plays a crucial part in the overall thermal resistance (Figure 13).

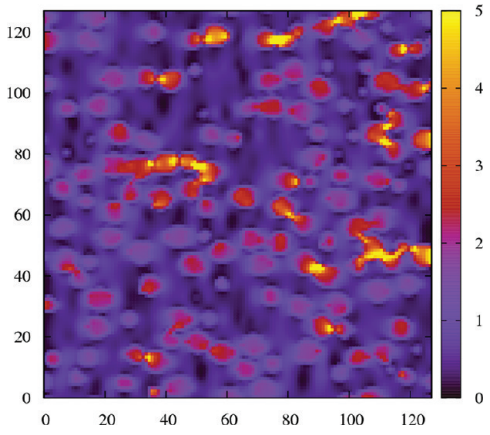

Figure 13. Magnitude of heat flux at steady state is shown on the *xy* cross section of a three-dimensional spherical particulate composite system where 2304 spherical high conductivity fillers are dispersed in the lower conductivity matrix. The filler volume fraction 30%. The unit of length is δx. Temperature gradient is applied along the horizontal direction, x, by imposing the fixed temperature boundary condition at $x = 0\ \delta x$ and $x = 128\ \delta x$. The heat flux along x direction is shown as divided by the average heat flux. Filler materials have the phonon mean free path of 30 δx, whereas the matrix material has zero phonon mean free path. $k_f = 30k_m$ and $\eta_m = 4\ \delta x$ at the interface between the filler and the matrix. Interface resistance is not applied between touching fillers. Amplified heat flux is shown along the filler agglomerate.

5. EXPERIMENTAL APPROACHES TO TAILOR THERMAL TRANSPORT IN NANOCOMPOSITES

The modeling schemes, molecular to microscopic scale, discussed in prior sections (sections 2−4) outline potential approaches of tailoring thermal properties at different scales. The computational predictions provided processing guidelines for developing the experimental approaches. In this section, two representative experimental studies are discussed to address the issue of tailoring thermal transport in polymeric composites by modifying interface thermal resistance. This issue is discussed by two different routes:

(1) Dispersing and functionalizing highly thermally conductive fillers in the polymeric matrix,
(2) Developing highly conductive anisotropic thermal interface materials.

5.1. Dispersion and Functionalization of Highly Thermally Conductive Fillers in the Polymeric Matrix.

It is well-known that polymers have very low thermal conductivity and are not suited for the design demands in many thermal management related aerospace applications. Several research studies have suggested that dispersing and functionalizing nanofillers could improve the effective thermal conductivity of the polymeric composites.[51−54] The fillers may either be in the form of fibers or in the form of particles uniformly distributed in the polymer matrix. While the thermophysical properties of fiber-filled composites are anisotropic (except for the very short, randomly distributed fibers), they are isotropic for particle-filled polymers. The detailed discussion of previous research efforts has been reported elsewhere.[55]

Exfoliated graphite platelets are an alternative promising filler material for improving the thermo-mechanical properties of the polymeric matrix. In the 1910s, Aylsworth[56] developed and proposed expanded graphite as reinforcement of polymers. Lincoln et al.,[57] in the 1980s, proposed the dispersion of intercalated graphite in polymeric resins by conventional composite processing techniques. Since then, significant research has been conducted on exfoliated graphite reinforced polymers using graphite particles of various dimensions and a wide range of polymers. As a few examples, Drzal et al.[53] demonstrated the use of exfoliated graphite platelets to enhance the thermal and mechanical properties of polymeric resins. Lafdi et al.[58] dispersed exfoliated graphite flakes in an epoxy resin and observed a twenty-4-fold increase in thermal conductivity for the 20% graphite flake composite as compared to the pure resin. Ma et al.[59] studied the effect of silane functionalization of multiwall CNTs on properties of epoxy composites indicated that grafting silane molecules improved the dispersion of the nanotubes in epoxy resin thereby improving the interfacial interactions, mechanical and thermal properties. This representative study focuses on the chemical treatment of graphite flakes to make them compatible with the epoxy system and study the effective thermal, electrical, and flow properties of the resultant composites.

In this study, chemically functionalized exfoliated graphite-filled epoxy composites were prepared with load levels from 2 to 20% by weight. Exfoliated graphite (EG) flakes were supplied by Graftech International Ltd., Parma, OH. The details of graphite exfoliation are reported elsewhere[56] Epon 862/Epicure W was chosen as the model polymeric system for this study. An accelerating agent, Epicure 537, composed of organic salts was used to accelerate the curing reaction. Use of

an accelerator in the curing reaction helped in "locking in" the dispersed morphology by enhancing the rate of the curing reaction. The exfoliated graphite sheets were dispersed in the epoxy using a Flacktek Speedmixer.

5.1.1. Chemical Modification of the Exfoliated Graphite Flakes. The grafting reaction was carried out in a mixture of water/ethanol (25/75 by volume). A quantity of 3 g of γ-APS (3 aminopropoxyltriethoxy silane) was first introduced into 1000 mL of the mixture of water/ethanol, and the temperature was kept at 80 °C. Then, 10 g of exfoliated graphite was added into the above-mentioned solution, and the grafting reaction was realized, under shearing, for 5 h at 80 °C. The reaction product was filtered and washed six times using a mixture of water/ethanol and freeze-dried. The resultant product was ground and placed in a sealed container for characterization. X-ray photoelectron spectroscopy (XPS) of the grafted graphite flakes was performed to verify the grafting of the amine groups on the graphite flakes.

Compositional analyses, functionalization of the exfoliated graphite, were made with an XPS system operated at a pressure of 8×10^{-10} Torr. Binding energy positions were calibrated using the Au $4f_{7/2}$ peak at 83.93 eV and the Cu 3s and Cu $2p_{3/2}$ peaks at 122.39 and 932.47 eV_o, respectively. The results of the XPS study are presented in Figures 14 and 15.

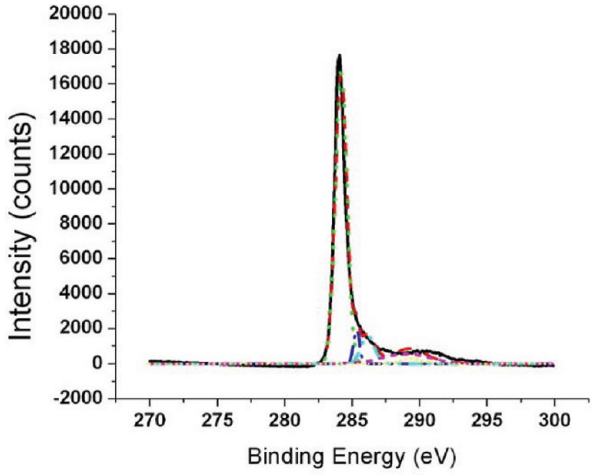

Figure 14. C1s spectrum for the expanded graphite flakes.

Figure 14 shows the C1s spectrum for the as-received expanded (exfoliated by Graftech International) graphite flakes. The C1s peak can be deconvoluted into four fitting curves. Peaks at 284.18, 285.28, 286.1, and 286.7 eV were observed. The respective percentages are presented in Table 1. Evidence of −COO, −C═O and C−O bonds in the C1s spectrum may be attributed to the oxidation of the graphite flakes as a result of the treatment with strong acids during the exfoliation procedure. The atomic compositions of the as-received oxidized graphite flakes are presented in Table 2.

The C1s spectrum and N1s spectrum for the silane modified graphite flakes are presented in Figure 15. The C1s spectrum for the amine silane modified graphite flakes showed a similar spectrum to the unmodified one; however a new peak attributed to Si−C appeared at 282.8 eV with an elemental composition of silicon at 3.4%. The Si−C peak confirms the presence of the silane on the graphite flakes after the treatment with the amine silane. The C1s spectrum for the silane-modified graphite flakes may be deconvoluted into six peaks at

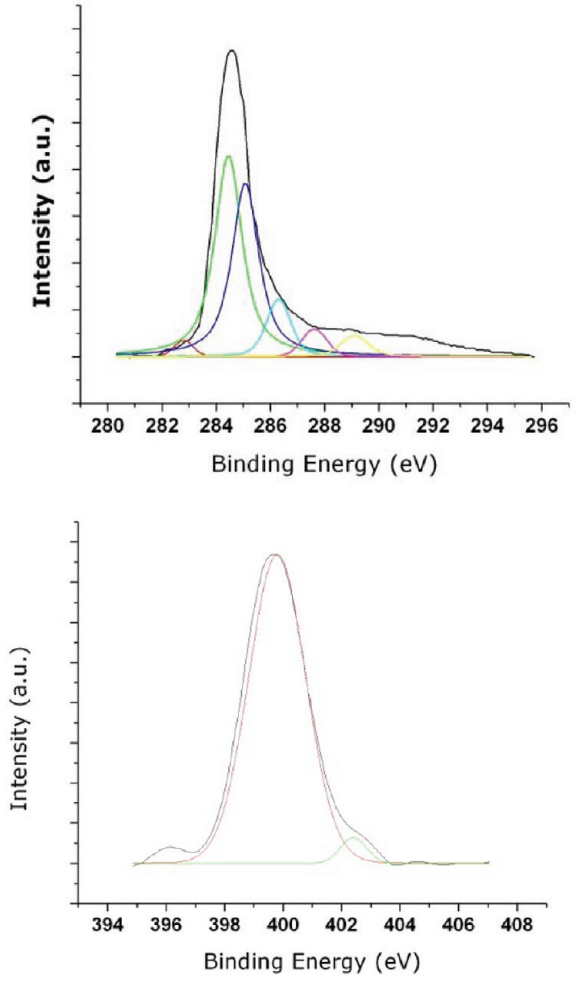

Figure 15. C1s and N1s spectra for the silylated graphite flakes.

Table 1. Summary of the Relative Percentage of the Carbon and Respective Assignation

	Relative Percentage of Carbon (%)					
	Si−C	C_g sp^2	C_d sp^3	C−O	−C═O	CO−O
BE (eV)	282.8	284.18−284.5	285.1−285.3	286−286.5	287.6−287.8	289−289.4
oxidized	0	74.2	4.4	8.1	0	13.3
silylated	3.4	65.7	5.2	11	4.9	9.8

Table 2. Summary of the Relative Percentage of the Carbon and Respective Assignation

	Element (at %)			
	C	O	N	Si
oxidized	94.35	5.65	0.0	0.0
silylated	83.89	10.5	2.31	3.3

282.8, 284.18, 285.16, 286.2, 287.78, and 289.2 eV. The respective percentage compositions of the individual peaks are presented in Table 1. From Table 1, the peak at 284.18 eV is attributed to elemental carbon (sp^2). The N1s spectrum for the modified graphite flakes presented in Figure 15 can be deconvoluted into two peaks at 399.8 and 402.4 eV, respectively. The predominant peak at 399.8 eV is attributed to a compound of nitrogen, silicon, carbon and oxygen. The Si 2p spectrum for the silylated graphite flakes is presented in Figure 16. The Si 2p

dx.doi.org/10.1021/am201496z | ACS Appl. Mater. Interfaces 2012, 4, 545−563

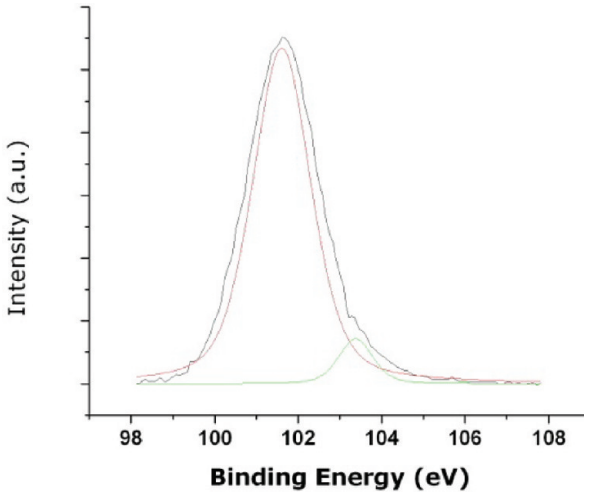

Figure 16. Si 2p XPS spectrum of silylated graphite flakes.

peak can be deconvoluted into two peaks. The first one at 101.6 eV represents the bonding between silicon and oxygen. The second peak at 103.3 eV may be attributed to the siloxane resulting from hydrolysis of the amine silane molecule as part of the silylation reaction. The N 1s peak shows the presence of protonated amine at 399.8 eV resulting from the chemisorption of the amine silane. A schematic of the reaction scheme for the silylation of the graphite flakes is presented in Figure 17.

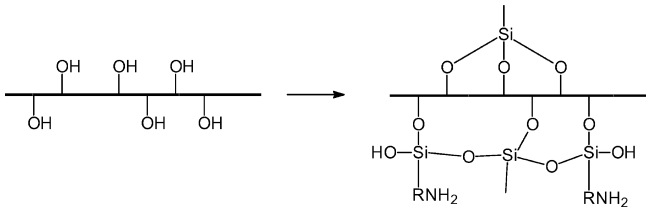

Figure 17. Schematic of the silane treatment of the graphite flakes.

The electron-rich nitrogen present in the amino silane enters into hydrogen bonding with the hydrogen donating oxidized carbon group on the graphite surface created by the acid treatment. It is assumed that the amino groups of the chemisorbed graphite flakes (due to silane coupling agent APS) react with the epoxy moieties of the resin in a manner similar to the reaction between epoxy and an amine-based hardener in the bulk phase.

5.1.2. Processing and Characterization of Composites. Differential scanning calorimetry (DSC) was employed to determine the amount of accelerator to be used and also to identify the processing window for dispersion of the nano-constituents in the resin. DSC scans were run on ~10 mg samples enclosed in hermetically sealed Al pans. The samples were heated from room temperature to 300 °C at a 5 °C/min heating rate. The DSC scans are shown in Figure 18. The cross-linking reaction of the epoxy curing is characterized by an exotherm peak in the DSC heat flow curve. The onset point of the exotherm corresponds to the gelling or the onset of the first cross-linking. At that point, the morphology gets "locked-in." Thus, the processing window has to be chosen at a temperature below the gel-point of the thermoset polymer. On the basis of the DSC scans, it was determined that the dispersion could be carried out at 60 °C with 3% accelerator without the risk of starting the curing reaction. In order to test this, an isothermal DSC experiment at 60 °C was performed. It was observed that

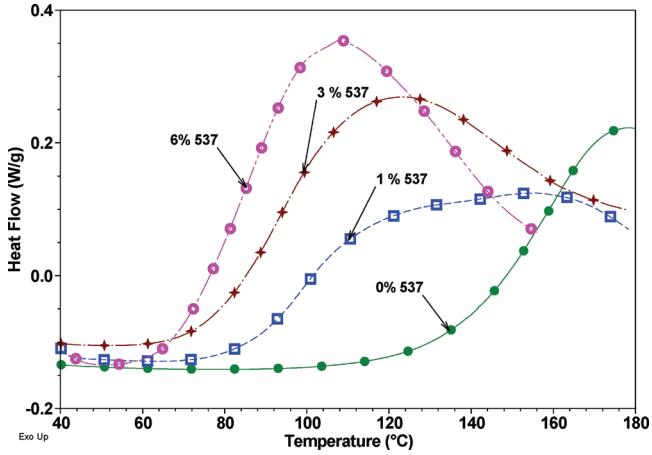

Figure 18. DSC scans to determine optimal processing window.

there was no evidence of initiation of the epoxy curing reaction at 60 °C even after 120 min. The mixing protocol for the synthesis of all the composites was as follows – Epon 862 and fillers were mixed in the Flacktek mixer @ 2800 rpm for 8 min. Subsequently, the Epicure W along with the Epicure 537 was mixed @ 1000 rpm for 30 s. Two sets of specimens, one with as-supplied graphite flakes (EXF) and the other with chemically treated graphite flakes (FN), were synthesized. The loading levels of the graphite platelets were 2, 4, 8, 16, and 20 wt % of the epoxy resin.

5.1.3. Rheology of the Composites. Rheology of the composites was performed on an advanced rheometrics expansion system (ARES) equipped with a forced convection oven. ARES is a mechanical spectrometer that is capable of subjecting a sample to either a dynamic or steady shear strain deformation and then measuring the resultant torque expended by the sample in response to this shear strain. Shear strain is applied by the motor, and the torque is measured by the transducer. For a set strain amplitude and frequency, actual sample deformation is determined by the measured motor and transducer displacement. The flow properties of the composites were measured in a parallel plate mode at an angular frequency of 6.28 Hz. The strain exerted on the specimens was 3%, and the temperature range investigated was 35 – 250 at 5 °C/min. For a polymer to qualify for vacuum-assisted resin transfer molding (VARTM), the viscosity has to be less than 3000 cP. The processing window for polymers is the range of temperature over which the viscosity remains in the processing regime. The results of the rheology test are presented in Figure 19. From the rheology plot, it was observed that the pure polymer has a viscosity of ~32 cP at 75 °C. Composites formulated of the unfunctionalized graphite exceed this viscosity range for any loading level above 2 wt %. For the functionalized graphite, the 2 wt % and the 4 wt % fall within the processing window of the VARTM process. The functionalized graphite-based composites perform better than the unfunctionalized ones in this figure of merit. Both the 2 and 4 wt % functionalized composites have a longer processing window than the 2 wt % unfunctionalized graphite composites.

5.1.4. Thermal Conductivity Characterization. The heat capacity and thermal conductivity of the specimens were measured by the Netzsch laser flash diffusivity system, LFA 457. The flash parameters used for this experiment were a laser voltage of 1922 V, 100% open filter. These laser parameters resulted in an approximate laser energy of 6.13 Joules incident

dx.doi.org/10.1021/am201496z | ACS Appl. Mater. Interfaces 2012, 4, 545–563

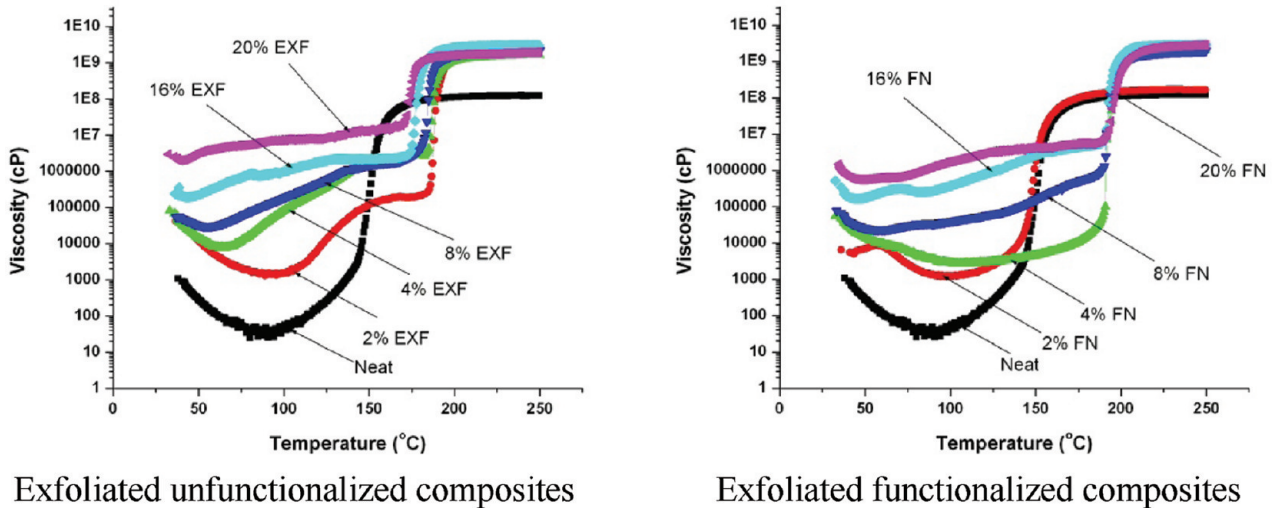

Figure 19. Viscosity profiles for the unfunctionalized and functionalized graphite composites.

on the specimen surface. The reference used for the heat capacity calculation was a 5-mm-thick specimen of POCO graphite. The reference sample was also coated with a thin layer of graphite. This instrument and methodology conform to ASTM E1461−92, "Standard Test Method for Thermal Diffusivity of Solids by the Flash Method" for the measurement of thermal diffusivity. The result of the thermal diffusivity test is presented Table 3.

Table 3. Results of the Thermal Diffusivity Experiment

specimen	C_p (J/g-K)	diffusivity (mm^2/s)	K W/m-K
neat	1.06	0.157	0.195
FN2	0.966	0.267	0.303
FN4	0.966	0.384	0.443
FN8	1.000	0.993	1.235
FN16	1.000	2.644	3.268
FN20	1.177	4.152	5.864
EXF2	0.779	0.278	0.26
EXF4	0.8	0.342	0.319
EXF8	0.733	0.582	0.578
EXF16	0.801	2.459	2.267
EXF20	0.703	4.1501	4.265

The thermal conductivities of the different specimens as measured by the LFA 457 have been plotted and are reported in Figure 20. The thermal conductivity of the pure Epon 862/W epoxy resin is around 0.2 W/m-K. The thermal conductivity of the epoxy resin barely changes with the addition of 2 and 4% untreated exfoliated graphite flakes. At 8% loading, the thermal conductivity increases from 0.2 W/m-K to 0.5 W/m-K. As the filler concentration is further increased to 16%, the thermal conductivity increases 9-fold to ~2 W/m-K.

Thermal conductivity increases 19-fold compared to the pure resin (0.2 W/m-K to 4 W/m-K with a filler concentration of 20%. The thermal properties of the chemically modified graphite flake composites exhibit similar behavior to the untreated composites at low filler levels (until 4% loading). At 8% filler concentration, the thermal conductivity value of the treated composites is nearly double that of the untreated composites. A similar improvement in thermal conductivity is noted for all the higher concentrations of the treated graphite flake composites. Addition of 20% treated graphite flakes in the

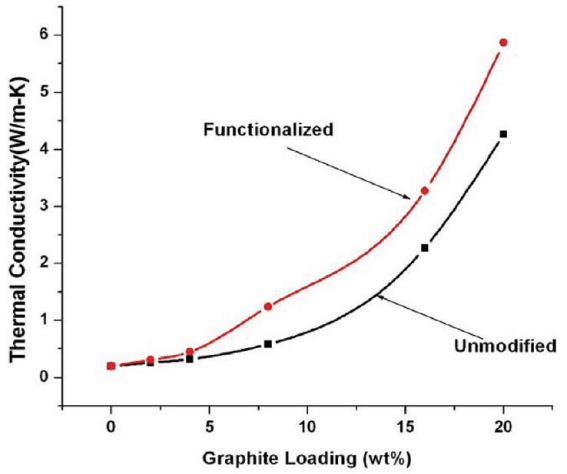

Figure 20. Thermal conductivity plot for the graphite - epoxy composite.

epoxy resin increases the thermal conductivity of the epoxy resin to 5.8 W/m-K − a 28-fold improvement. Debelak et al.[58] reported the thermal conductivity of exfoliated graphite-epoxy composites with graphite fillers of three different sizes. In their study, they used filler sizes of 297, 150, and 90 μm. The highest thermal conductivity achieved in that study at 20% filler loading for all the different sizes was 4.3 W/m-K. That corresponds well with the thermal conductivity results of the untreated graphite composites used in this study. In comparison, the silylated graphite composites at 20% loading level had a thermal conductivity of 5.8 W/m-K, a 35% increase due to the silylation of the graphite flakes.

In summary, the above experimental investigation shows how functionalization can help in increasing the effective thermal conductivity of nanocomposites by reducing interface thermal resistance at the graphite/polymeric interface and is in full agreement with the modeling studies discussed before. XPS studies revealed that chemically functionalizing the nanoparticles made them form covalent bonds with the matrix thereby increasing the thermal conductivity of the overall system. Though dispersing functionalized, thermally conductive nanoparticles in the polymeric matrix increased the thermal conductivity 21-fold,

dx.doi.org/10.1021/am201496z | ACS Appl. Mater. Interfaces 2012, 4, 545−563

the processability, as measured by the viscosity increased, rendering the system outside the processing window.

5.2. Development of Highly Conductive Anisotropic Thermal Interface Materials. Thermal Interface Materials (TIM) used for efficient heat dissipation from electronic components is gaining increased attention. Thermal conducting pads made with various conductive fillers are widely used commercially. CNTs, with their exceptional thermal properties, are an ideal candidate for TIM applications. For example, Huang et al. have developed TIM based on aligned carbon nanotubes embedded in an elastomer.[60] Though they achieved a 120% enhancement of thermal conductivity using the nanocomposite film, the achieved value of 1.21 W/m-K was much less than the theoretical thermal conductivity of aligned carbon nanotubes. Besides TIM, the through-thickness thermal conductivity in adhesive joints is very low, often limited by the low thermal conductivity of the resin used as well as interfacial imperfections. Thus, in an effort to enhance the heat transfer efficiency at thermal interfaces, our recent study is discussed, incorporating vertically aligned carbon nanotubes to improve the through-thickness thermal conductivity in adhesive joints.

For this representative study, multi walled carbon nanotube (MWCNT) films were grown on silicon substrates by chemical vapor deposition. The aligned CNT films were prepared by pyrolyzing iron(II) phthalocyanine under Ar/H_2 at 900 °C as described in detail elsewhere.[61,62] The average diameter of the tubes was 30 nm and the average height of the MWCNT film was 30 μm. Figure 21 shows the scanning electron micrograph of the as-produced MWCNT film. It is clear that as grown, aligned nanotubes are not perfectly aligned vertically. Though the vertical alignment of the nanotubes is evident from the SEM image, there are some obvious regions of imperfections, specifically bent tubes.

5.2.1. Experimental Development of the Thermal Interface Material. The wafer with the MWCNT side facing upward was dipped in a beaker containing a 10% Epon 862/W−acetone solution. The film was then kept in a vacuum oven at 60 °C for 2 h for the solvent to escape. The epoxy was then cured at 177 °C for 2 h. Figure 22 shows a cross-sectional view of the MWCNT film infused with the epoxy. The epoxy−MWCNT film was then peeled off the quartz substrate by etching with a 10% HF solution. The nanotube tips were exposed selectively by etching the film surface with 32 W RF oxygen plasma for 30 min. SEM images of the film after the plasma etching are shown in Figure 23. It can be observed from Figure that the nanotube tips are clipped due to the plasma etching. The side of the film which was previously anchored to the substrate was similarly etched in O_2/Ar RF plasma under the above-mentioned conditions.

Next, a 900 Å layer of gold was thermally evaporated on both sides of the film. Highly oriented pyrolytic graphite (HOPG) adherent face sheets were sputter-coated with Au−Pd for 3 min. Then, a thin layer of Indium metal was melt-coated on the graphite adherents' surfaces and the epoxy-nanotube film (served as a transition zone). Finally, the epoxy-nanotube film was sandwiched between the graphite face sheets and fused together by heating at 175 °C. A schematic of the assembled device is shown in Figure 24.

5.2.2. Thermal Transport Characterization. Bulk thermal diffusivity measurements were measured using a Netzsch Laser Flash apparatus under nitrogen purge. The laser flash technique allows measuring the thermal diffusivity (h) of solid materials over a temperature range of −180 to 2000 °C. The laser flash (or heat pulse) technique consists of applying a short duration (<1 ms) heat pulse to one face of a parallel-sided sample and

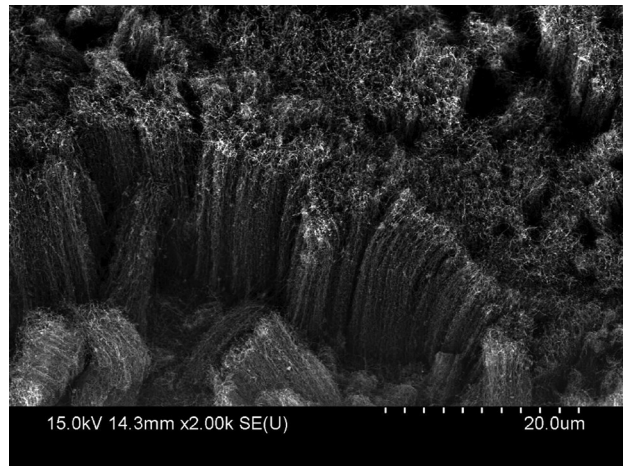

Figure 21. SEM micrograph of cross-section of as produced MWCNT Film.

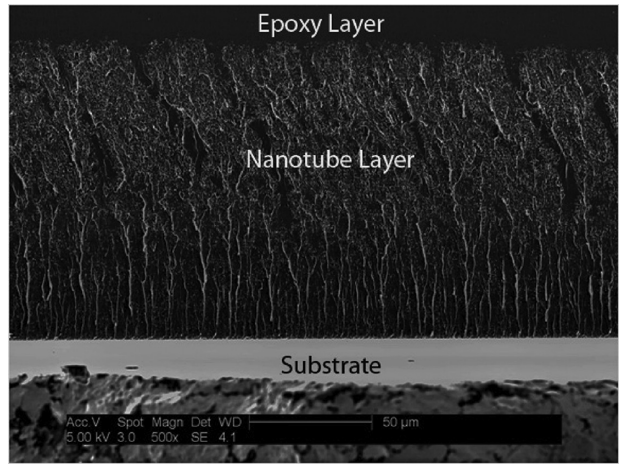

Figure 22. SEM micrograph of cross-section of epoxy-infused MWCNT film before plasma etching.

monitoring the temperature rise on the opposite face as a function of time. This temperature rise is measured with an infrared detector. A laser is used to provide the heat pulse.

The thermal diffusivity is measured as

$$h = \frac{\varpi}{\pi}\frac{L^2}{t_{1/2}} \tag{21}$$

where, ϖ is a constant, L is the thickness of the specimen and $t_{1/2}$ is the time for the rear surface temperature to reach half its maximum value. Thermal conductivity can be obtained from the laser flash measurements by knowing the heat capacity at constant pressure (C_p) and the density (ρ) of the specimen and is given by

$$k = C_p \cdot \rho \cdot h \tag{22}$$

The heat capacity of the samples was measured with the laser flash method by comparing the temperature rise of the sample to the temperature rise of a POCO graphite reference sample of known specific heat, tested under the same conditions. Heat capacity was calculated on the basis of eq 23.

$$C_{p,\,\mathrm{sample}} = \frac{(mC_p\Delta T)_{\mathrm{ref}}}{(m\Delta T)_{\mathrm{sample}}} \tag{23}$$

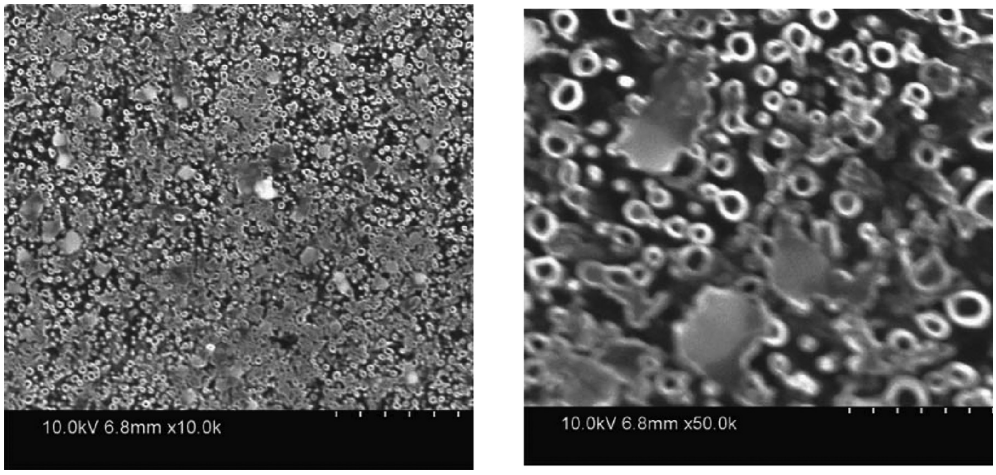

Figure 23. SEM micrograph of epoxy-NWCNT film after plasma etching (View normal to MWCNT film plane).

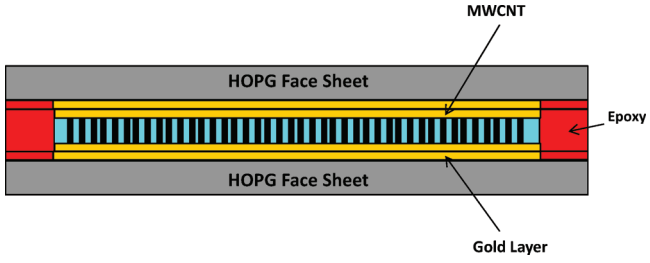

Figure 24. Schematic view of the assembled device.

The length, width, height, and weight for the different samples were accurately measured. Densities of the samples were calculated on the basis of the ratio of the measured weight to measured volume. Based on the heat capacity and thermal diffusivity measurements, the thermal conductivity for the device and a graphite reference was determined at 24 °C, from eq 22 above. Four sets of samples were evaluated, the HOPG face-sheet, HOPG layers bonded by epoxy, HOPG layers bonded by indium, and HOPG layers bonded by indium with the modified MWCNT film in between. The thermal conductivity values for the samples measured are presented in Figure 25. The measured

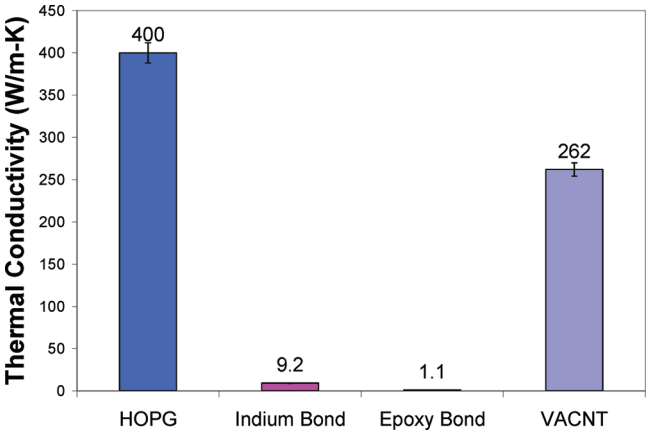

Figure 25. Thermal conductivities of measured samples.

thermal conductivities for the graphite face sheet, the face sheets bonded by epoxy adhesive, face sheet bonded by Indium, and the actual device were found to be 400, 1.1, 9.2, and 262 W/m-K, respectively.

Summarizing the effort, by engineering the interface in the adhesively bonded joint, excellent through-thickness thermal conductivity was achieved for the developed device. The diffusion bonding between the gold-coated nanotube tips, the indium and the gold-coated graphite face sheets resulted in lowering of the thermal interfacial resistance thus enhancing the interfacial thermal transport.

6. CONCLUSIONS

The effective thermal properties of polymeric composite materials are often dictated by the interface thermal resistance. Modeling (atomistic, meso- and microscale) and experimental approaches to address the thermal composite were discussed. For the matrix phase thermal property estimates, both equilibrium and nonequilibrium molecular dynamics simulation methods were reviewed to estimate the thermal conductivity for the epoxy system. The analysis of the different contributions toward the heat flux autocorrelation function suggested that virial contributions from nonbonded van der Waals interactions dominate the thermal conductivity with negligible contributions from bonded and electrostatic interactions. Given the dominant contribution of van der Waals interactions, the higher thermal conductivity of the epoxy network (compared to its uncross-linked counterparts) is attributed to the densification of the network during cross-linking, which enhances neighboring nonbonding interaction. When carbon nanotubes are added as filler to an epoxy matrix, the Kaptiza conductance in the filler–matrix interface was found to follow a linear increase with the degree of functionalization up to 2.5% CNT functionalization. However, the sidewall functionalization of CNT, as structural defects, is also expected to lower the through-axis thermal conductivity of CNT.

At the composite level (i.e., at the microscopic scale of fibers embedded within the matrix phase), micromechanical models with regular and randomly distributed fibers were developed for the study of transverse thermal conductivity of laminated composites. Both analytical and numerical FE solutions were reproduced and reinvestigated. A parametric study was conducted by varying wide ranges of fiber volume fractions and fiber-to-matrix thermal conductivity ratios. The numerical solutions were compared with the analytical solutions from the simple rule of mixture (SROM), enhanced rule of mixture (EROM), and the more advanced equivalent inclusion method (EIM). Compared with FE solutions, it was found that the EIM

dx.doi.org/10.1021/am201496z | ACS Appl. Mater. Interfaces 2012, 4, 545–563

yields a reasonably agreeable solution with the hexagonal-array FE solution for wide ranges of fiber volume fraction and fiber-to-matrix thermal conductivity ratios. The hexagonal-array model represents the composite microstructure more closely than other fiber distribution models, and thus the EIM can be useful to quickly obtain a reasonable solution without the FE calculation in predicting not only the transverse thermal conductivity, but other physical transverse properties of the laminated composites including the transverse modulus, transverse electrical conductivity, etc. The randomness of the fiber distribution in composites was studied by building the random fiber model. Comparison of the results with regular-fiber models indicates that the transverse thermal conductivity of composites can significantly be affected by the random fiber distributions, especially at high volume fraction. In this case, the random fiber solutions consistently yield higher conductivity than the idealized regular fiber ones up to a practical upper bound of the fiber packing density in composites. It was shown that the predictions with the random fiber distribution agree well with the experimental data, which indicated the effect of the random fiber distribution can be a reason for the under-prediction of the experimental data compared with the unitcell model predictions. The effective transverse thermal conductivity is significantly influenced not only by the properties of fiber and matrix constituents and volume contents, but also randomness of the fiber distributions.

In the less-than-micro spatiotemporal scale of the current devices of interest in industry (i.e., mesoscale), heat transfer modeling needs to consider the effects of the finite phonon mean free path and the interface thermal resistance. On the basis of the linear relaxation of the nonequilibrium phonon distribution toward local equilibrium, the lattice Boltzmann Peierls Callaway (LBPC) equation, with its recently proposed mesoscopic phonon interface collision rule, can realize the finite phonon mean free path and multiphase phonon gas with interface thermal resistance. In the Callaway collision operator, the Umklapp collision relaxation time determines the phonon mean free path, while the interface collision relaxation time determines the Kapitza length, hence the Kapitza resistance. The highly parallelizable LB numerical scheme enables the LBPC equation to model large scale simulations efficiently. In view of multiscale integration, it is worth mentioning that the atomistic scale predictions of the interface resistance (or conductance) are needed as input to the LBPC equation to enable mesoscale predictions.

Experimentally, along the direction of what was observed computationally and in order to enhance the thermal conductivity of polymeric composite systems, two different routes were implemented. In the first instance, to enhance the thermal properties of the matrix phase, chemically functionalized nanoparticles were dispersed in the epoxy matrix. It was observed that chemically functionalizing the nanoparticles made them form covalent bonds with the matrix thereby increasing the thermal conductivity of the overall system. Though dispersing functionalized thermally conductive nanoparticles in the polymeric matrix increased the thermal conductivity by 21-fold, the composite processability, as measured by the viscosity, increased significantly, rendering the composite system outside the processing window. The second effort was focused on developing highly conductive anisotropic thermal interface materials. By engineering the interface in the adhesively bonded joint, excellent through-thickness thermal conductivity was achieved. The diffusion bonding between the gold coated nanotube tips, the indium and the gold-coated graphite face sheets resulted in lowering the thermal interfacial resistance, thus enhancing the interfacial thermal transport.

■ ASSOCIATED CONTENT

Ⓢ Supporting Information

Chronological list of abbreviations and usage the symbols that are used in this article. This material is available free of charge via the Internet at http://pubs.acs.org/

■ AUTHOR INFORMATION

Corresponding Author

*E-mail: Ajit.Roy@wpafb.af.mil (A.K.R.); Barry.Farmer@wpafb.af.mil (B.L.F.).

Notes

The authors declare no competing financial interest.

■ ACKNOWLEDGMENTS

The authors are grateful to Air Force Office of Scientific Research (Lab Tasks: 2302BR7P, 2306AR8P, 2306CR9P) for the funding support. The authors also thank Dr. Jennifer Wohlwend for the thorough, critical reading, and her suggestions regarding the manuscript.

■ REFERENCES

(1) Biercuk, M. J.; Llagano, M. C.; Hyun, J. K.; Johnsond, A. T.; Fischer, J. E. *Appl. Phys. Lett.* **2002**, *80*, 2767−2769.
(2) Liu, C. H.; Huang, H.; Wu, Y.; Fan, S. S. *Appl. Phys. Lett.* **2004**, *84*, 4248−4250.
(3) Huang, H.; Liu, C.; Wu, Y.; Fan, S. *Adv. Mater.* **2005**, *17*, 1652−1656.
(4) Cahill, D. G.; Ford, W. K.; Goodson, K. E.; Mahan, G. D.; Majumdar, A.; Maris, H. J.; Merin, R.; Philpot, S. R. *J. Appl. Phys.* **2003**, *93*, 793−818.
(5) Kubo, R.; Toda, M.; Hashitsume, N.; Saito, N. *Statistical Physics II*, Springer: Berlin, 1985.
(6) Motoyama, S.; Ichikawa, Y.; Hiwatari, Y.; Oe, A. *Phys. Rev. B.* **1999**, *60*, 292−298. Bernu, B.; Vieillefosse, P. *Phys. Rev. A* **1978**, *18*, 2345−2355. Nijboer, B. R. A.; De Wette, F. W. *Physica (Utrecht)* **1957**, *23*, 309−321.
(7) Anderson, C. V. D. R.; Tamma, K. K. *Int. J. Numer. Methods Heat Fluid Flow* **2004**, *14* (1), 12−65.
(8) Muller-Plathe, F. *J. Chem. Phys.* **1997**, *106*, 6082−6085.
(9) Varshney, V.; Patnaik, S. S.; Roy, A. K.; Farmer, B. L. *Macromolecules* **2008**, *41*, 6837−6842.
(10) Varshney, V.; Patnaik, S. S.; Roy, A. K.; Farmer, B. L. *Polymer* **2009**, *50*, 3378−3385.
(11) Dauber-Osguthorpe, P.; Roberts, V. A.; Osguthorpe, D. J.; Wolff, J.; Genest, M.; Hagler, A. T. *Proteins: Struct., Funct. Genet.* **1988**, *4*, 31−47.
(12) Ganguli, S.; Roy, A. K.; Anderson, D. P. *Carbon* **2008**, *46* (5), 806−817.
(13) Shenogin, S.; Bodapati, A.; Keblinski, P.; McGaughey, A. J. H. *J. Appl. Phys.* **2009**, *105*, 034906.
(14) Bresme, F.; Hafskjold, B.; Wold, I. *J. Phys. Chem.* **1996**, *100*, 1879−1888.
(15) Kapitza, P. L. *Zh. Eksp. Teor. Fiz.* **1941**, *11*, 1.
(16) Varshney, V.; Patnaik, S. S.; Roy, A. K.; Farmer, B. L. *J. Phys. Chem. C* **2010**, *114*, 16223−16228.
(17) Springer, G. S.; Tsai, S. W. *J. Compos. Mater.* **1967**, *1*, 166−173.
(18) Chamis, C. C. *J. Reinf. Plast. Compos.* **1987**, *6*, 268−289.
(19) Zou, M.; Yu, B.; Zhang, D. *J. Phys. D* **2002**, *35*, 1867−1874.
(20) Benveniste, Y. *J. Appl. Phys.* **1987**, *61*, 2840−2843.
(21) Benveniste, Y.; Chen, T.; Dvorak, G. J. *J. Appl. Phys.* **1990**, *67*, 2878−2884.
(22) Benveniste, Y.; Miloh, T. *J. Appl. Phys.* **1989**, *66*, 176−180.
(23) Benveniste, Y.; Miloh, T. *J. Appl. Phys.* **1991**, *69*, 1337−1344.

(24) Benveniste, Y.; Miloh, T. *J. Mech. Phys. Solids* **1999**, *47*, 1873–1892.
(25) Miloh, T.; Benveniste, Y. *J. Appl. Phys.* **1988**, *63*, 789–796.
(26) Miloh, T.; Benveniste, Y. *Proc. R. Soc. London, Ser. A* **1999**, *455*, 2687–2706.
(27) Benveniste, Y. *Mech. Mater.* **1987**, *6*, 147–157.
(28) Hatta, H.; Taya, M. *J. Appl. Phys.* **1985**, *58*, 2478–2486.
(29) Hatta, H.; Taya, M. *Int. J. Eng. Sci.* **1986**, *24*, 1159–1172.
(30) Hatta, H.; Taya, M. *J. Appl. Phys.* **1986**, *59*, 1851–1860.
(31) Eshelby, J. D. *Proc. R. Soc. London, Ser. A* **1957**, *241*, 376–396.
(32) Rolfes, R.; Hammerschmidt, U. *Compos. Sci. Technol.* **1995**, *54*, 45–54.
(33) Nan, C.-W.; Birringer, R.; Clarke, D. R.; Gleiter, H. *J. Appl. Phys.* **1997**, *81*, 6692–6699.
(34) Nan, C.-W.; Shi, Z.; Lin, Y. *Chem. Phys. Lett.* **2003**, *375*, 666–669.
(35) Islam, M. R.; Pramila, A. *J. Compos. Mater.* **1999**, *33*, 1699–1715.
(36) Noor, A. K.; Shah, R. S. *Compos. Struct.* **1993**, *26*, 7–23.
(37) Hill, R. *J. Mech. Phys. Solids* **1965**, *13*, 213–222.
(38) Rayleigh, L. *Philos. Mag.* **1882**, *34*, 481–502.
(39) Duschlbauer, D.; Boehm, H. J.; Pettermann, H. E. *Mater. Sci. Technol.* **2003**, *19*, 1107–1114.
(40) Al-Nassar, Y. *Heat Mass Transfer* **2006**, *43*, 117–122.
(41) Sihn, S.; Roy, A. K. *J. Compos. Mater.* **2011**, *45*, 1245–1255.
(42) Thornburg, J. D.; Pears, C. D. *Prediction of the Thermal Conductivity of Filled and Reinforced Plastics.*; American Society of Mechanical Engineers: New York, 1965; ASME Paper 65-WA/HT-4.
(43) Swartz, E. T.; Pohl, R. O. *Rev. Mod. Phys* **1989**, *61*, 605–668.
(44) Guyer, R. A.; Krumhansl, J. A. *Phys. Rev.* **1966**, *148*, 766–778.
(45) Guyer, R. A.; Krumhansl, J. A. *Phys. Rev.* **1966**, *148*, 778–778.
(46) Majumdar, A. *J. Heat Transfer* **1993**, *115*, 7–16.
(47) Guyer, R. A. *Phys. Rev. E* **1994**, *50*, 4596–4608.
(48) Jianug, W.-S.; Ho, J.-R. *Phys. Rev. E* **2008**, *77*, 066710.
(49) Lee, J.; Roy, A. K.; Farmer, B. L. *Phys. Rev. E* **2011**, *83*, 056706.
(50) Callaway, J. *Phys. Rev.* **1959**, *113*, 1046–1051.
(51) Bagchi, A.; Nomura, S. *Compos. Sci. Technol.* **2006**, *66*, 1703–1712.
(52) Chang, T. E.; Kisliuk, A.; Rhodes, S. M.; Brittain, W. J.; Sokolov, A. P. *Polymer* **2006**, *47* (22), 7740–7746.
(53) Kalaitzidou, K.; Fukushima, H.; Drzal, L. T. *Compos. Sci. Technol.* **2007**, *67*, 2045–51.
(54) Luyt, A. S.; Molefi, J. A.; Krump, H. *Polym. Degrad. Stab.* **2006**, *91* (7), 1629–36.
(55) Ganguli, S.; Anderson, D. A.; Roy, A. K. *Carbon* **2008**, *46* (5), 806–817.
(56) Aylsworth, J. W., U.S. Patent 1 137 73, 1915.
(57) Lincoln, V. F., Claude, Z., U.S. Patent 4 414 142, 1983.
(58) Debelak, B.; Lafdi, K. *Carbon* **2007**, *45*, 1727–1734.
(59) Ma, P. C.; Kim, J. K.; Tang, B. Z. *Compos. Sci. Technol.* **2007**, *67* (14), 2965–72.
(60) Huang, H.; Liu, C.; Wu, Y.; Fan, S. *Adv. Mater.* **2005**, *17*, 1652–1656.
(61) Ganguli, S.; Sihn, S.; Roy, A. K.; Dai, L.; Qu, L. *J. Nanosci. Nanotechnol.* **2009**, *9*, 1727–1733.
(62) Sihn, S.; Ganguli, S.; Roy, A. K.; Qu, L.; Dai, L. *Compos. Sci. Technol.* **2008**, *68*, 658–665.